DART radiative transfer modelling for sloping landscapes

Ying-Jie Wang, Nicolas Lauret, Jean-Philippe Gastellu-Etchegorry

DART radiative transfer modelling for sloping landscapes

Yingjie WANG[1], Nicolas Lauret[1], Jean-Philippe Gastellu-Etchegorry[1]

[1] CESBIO, CNES-CNRS-IRD-UPS, University of Toulouse, 31401 Toulouse CEDEX 09, France

Correspondence to: Yingjie WANG (yingjiewang1102@gmail.com)

Abstract

Topography is one of the key factors that impact remotely sensed data and their interpretation. Indeed, combined with the viewing geometry and neighbour effects, it strongly affects the direct, diffuse and multi-scattered scene irradiance, which in turn impacts the radiative budget and remote sensing signals of the landscapes. The increased availability of digital elevation models (DEM) and the advancement of 3D radiative transfer (RT) models allow us to better address these topographic effects. DART (Discrete Anisotropic Radiative Transfer) is one of the most accurate and comprehensive 3D RT models that simulate remote sensing observations of natural and urban landscapes with topography and atmosphere. It simulates environmental effects (*i.e.*, impact of adjacent landscape on the observed landscape) using a so-called infinite slope mode that infinitely duplicates the observed landscape while ensuring the continuity of slope and altitude at the DEM edges. Up to DART version 5.7.4, this mode was slightly inaccurate and computer intensive, depending on the topography. This paper presents an innovative modelling strategy that greatly improves it in terms of accuracy, image quality and

computer efficiency. For that, a fictive auxiliary oblique plane, adapted to the landscape topography, is introduced for managing the scene illumination, the Earth-Atmosphere coupling and the storage of the radiation that exits the scene before being projected onto the sensor plane. Improvements and validations are illustrated both visually and quantitatively by DART images, radiometric products and radiative budget. For example, the observed reflectance of a Lambertian slope is equal to the expected analytical value. In addition, the solar plane reflectance of a forest on a mountain slope (experimental scene) has an average error of about 0.01% relative to the reflectance of the same forest stand in the reference scene (*i.e.*, nine duplications of the experimental scene). This new modelling is already integrated in the official DART version (https://dart.omp.eu).

Key words

Topography, DART, Infinite slope, Radiative transfer, Environmental effects

1 Introduction

Mountain regions cover around a quarter of the Earth's land surface (Liang, 2005) and are home to around one-tenth of the world's population (Denniston, 1996). They also provide vital economic and ecological resources to the world's population, thanks to their rich biodiversity, water-storing capacity, mineral reserve, *etc* (Price, 1998). Therefore, mountain areas are more and more surveyed with remote sensing (RS) data (Boori et al., 2015; Barrachina et al. 2015; Reinhold et al., 2016; Chimner et al., 2019). However, RS data are usually contaminated by topographic effects, since slopes combined with the observation configuration (*e.g.*, viewing

and sun geometry, atmosphere composition) impact the direct, diffuse and multi-scattered irradiance, which in turn affects the RS signals and radiative budget (RB) of mountain regions (Schaaf et al., 1994; Mousivand et al., 2015; Pellarin et al., 2016; Wen et al., 2018). In the last four decades, a lot of work has been done to eliminate or to reduce these topographic effects (Holben and Justice, 1980; Proy et al., 1989; Sandmeier et al., 1997; Richter and Schläpfer; 2011; Santini et al., 2019), notably through the development of numeric models (Table 1).

Table 1. Models that quantify topographic effects. Model category and references are indicated.

Model Category	Model Name	Model Reference
Empirical	Cosine Correction	Holben and Justice, 1980
	C correction	Teillet et al., 1982
	SCS	Gu and Gillespie, 1998
Geometric optical	GOMST	Schaaf et al., 1994
	GOST	Fan et al., 2013
3D radiative transfer	DART	Gastellu-Etchegorry et al., 1996; 2017
	LESS	Qi et al., 2018
	RAPID3	Huang, 2018
	Rayspread	Widlowski et al., 2007

Empirical models (*e.g.*, Cosine Correction, C correction, SCS) are the simplest and most practical for topographic correction, but the lack of generality and physical considerations limits their accuracy. Geometric optical models (*e.g.*, GOMST, GOST) use a geometric approach to quantify how canopy directional reflectance depends on slopes, solar direct irradiance and 3D tree crowns. However, they usually neglect sky diffuse illumination and multiple scattering in

63 landscapes. Also, the solo slope is a theoretical assumption that rarely exists in the nature. Being
64 more sophisticated and comprehensive, 3D radiative transfer (RT) models (*e.g.*, DART, LESS,
65 RAPID, Rayspread) are assumed to be the most accurate. They can simulate complex
66 topography, realistic 3D landscape elements, multiple scattering in the landscape and possibly
67 with diffused illumination from the atmosphere. Thanks to the development of computer
68 hardware and RT algorithms (*e.g.*, PBRT, LuxCoreRender, Mitsuba) (Grimaldi and Vergauwen,
69 2008; Jakob, 2014; Pharr et al., 2016), 3D RT models become more and more efficient, which
70 opens new opportunity for removing or reducing topographic effects in RS observations. Most
71 3D RT models were developed for the Earth surface RT modelling with atmosphere being
72 treated as an interface that is usually computed by an atmospheric RT model such as
73 MODTRAN (Berk and Hawes, 2017). It is typically the case of the recently developed LESS
74 model that can simulate very large forest landscapes (Qi et al., 2018). Atmospheric RT
75 modelling in presence of complex mountainous topography is still a challenge due to the
76 complex Earth-Atmosphere radiative coupling. To our knowledge, DART is the only 3D RT
77 model that simulates the Earth-atmosphere radiative coupling and environmental effects in
78 mountain areas. The so-called environmental effects are the impact of the adjacent landscapes
79 on the observed landscape.
80
81 The accuracy of DART Earth surface RT modelling for vegetation canopy over flat terrain was
82 already verified in the four phases of the RAMI project (RAdiative transfer Model
83 Intercomparison) (Widlowski et al., 2007; Widlowski et al., 2013; Widlowski 2015) and
84 experiments (Guillevic et al., 2003; Guillevic et al., 2013). DART atmospheric RT modelling
85 was successfully tested with MODTRAN5 simulations (Grau and Gastellu-Etchegorry, 2013;
86 Gastellu-Etchegorry et al, 2017; Wang and Gastellu-Etchegorry 2020), with reflectance
87 accuracy better than 0.004 and TIR brightness temperature accuracy better than 1.0 K, at bottom

88 (BOA) and top (TOA) of atmosphere. DART is continuously improved in terms of accuracy,
89 efficiency and modelling. For example, sun induced fluorescence modelling was introduced in
90 2016 (Gastellu-Etchegorry et al., 2017), and the Embree ray tracing library was recently
91 introduced for reducing simulation time and memory demand (Wald et al., 2014; Qi et al., 2019).
92 The work presented here is an improvement concerning RT modelling over sloping landscapes.
93
94 DART scene is a 3D array of cells that can contain turbid material, fluids and facets (*i.e.*,
95 triangles). The scene is either spatially finite (*i.e.*, "isolated scene" mode) or infinite (*i.e.*,
96 "repetitive scene" mode for simulating landscapes on flat terrain and "infinite slope" mode for
97 simulating landscapes on sloping terrain). A spatially infinite scene is an infinite repetition of
98 the actually simulated scene. Being designed for sloping landscapes, the infinite slope mode
99 ensures the altitude and slope continuity at the DEM edges of any duplicated scene. In DART,
100 RT is simulated by tracking rays along a finite number of discrete directions. The infinite slope
101 mode simulates the environmental effects by re-entering environmental rays into the observed
102 scene. These environmental rays are scattered from the neighbouring duplicated scenes. Rays
103 that exit the scene through its upper surface (*i.e.*, rays that constitute the observation) are spread
104 at their point of intersection with the horizontal plane at the scene bottom where they constitute
105 intermediate images, also called spread images (Yin et al., 2015). They are used to simulate the
106 Earth-atmosphere radiative coupling and RS images. The sloping topography explains that each
107 spread image has a specific polygon-shape and dimension per direction. Up to DART versions
108 5.7.4, scientists noted that the infinite slope mode could be inaccurate, as illustrated below in
109 this paper. An analysis of DART RT modelling allowed us to stress two major sources of
110 inaccuracy: (1) Scene illumination: depending on topography and illumination directions, it is
111 not uniform as expected. (2) Polygon-shape spread images: depending on topography and
112 viewing direction, these polygon-shapes can be very complex, which explains the presence of

113 border effects in simulated images and inaccurate Earth-Atmosphere radiative coupling. The
114 initial infinite slope mode was also constrained by technical issues: the required random access
115 memory (RAM) and simulation time could be unexpectedly large depending on the scene
116 topography. For example, compared to the simulation of an urban or vegetation landscape on a
117 horizontal surface, the simulation of this landscape on a 30° slope could increase the RAM
118 demand by a factor of 8, and computation time by a factor of 1.5.
119
120 This paper presents a new modelling strategy of DART infinite slope mode designed to improve
121 the accuracy and efficiency of DART RT modelling for sloping landscapes. Section 2 presents
122 major DART characteristics related to the present work. Section 3 describes the initial DART
123 infinite slope modelling method and its issues. Section 4 details the new infinite slope modelling
124 strategy, with additional information in the appendix. Section 5 firstly illustrates DART
125 improvements with simulations of a solo slope and a tree on a solo slope, and secondly presents
126 the validation of the new strategy with two simulated scenes: 1) a rugged slope, 2) a realistic
127 forest on a rugged slope. Finally, section 6 presents concluding remarks and perspectives.
128

129 ## 2 DART model and infinite slope mode

130 ### 2.1 General description

131
132 DART (https://dart.omp.eu) has been developed at CESBIO since 1992 (Gastellu-Etchegorry
133 et al., 1996; Gastellu-Etchegorry et al., 2017). It is one the most accurate and comprehensive
134 3D RT model in the optical remote sensing community. It simulates the RB, bi-directional
135 reflectance factor (BRF) and directional brightness temperature (BTF), images of
136 spectroradiometers at any altitude of 3D natural and urban landscapes, with topography and

atmosphere (Figure 1), for any viewing direction, from visible to thermal infrared domain. It simulates also the sun induced chlorophyll fluorescence of 3D vegetation canopies and the terrestrial and aero-spatial LiDAR signal (point cloud, waveform, photon counting).

In DART, the atmosphere is a layered horizontally homogeneous volume (Figure 1). A SQL database stores the spectral optical properties and vertical profiles of its constituents (*i.e.*, gases, aerosols, clouds). The Earth scene (*i.e.*, urban / vegetation landscape) is an array of cells (*i.e.*, voxels) (Figure 1) where elements are made of facets, also called triangles, possibly combined with cells filled with turbid vegetation medium or fluids (air, soot, water, *etc*). SQL databases store optical properties that can be assigned to scene elements. The integrated PROSPECT / FLUSPECT leaf model (Jacquemoud et al., 1990; Vilfan et al., 2016; Feret et al., 2017) computes leaf optical properties and fluorescence using leaf biochemistry and structure. Orthographic and perspective (pinhole, pushbroom, fisheye) cameras are also simulated in order to generate satellite, airborne and in-situ RS images (Yin et al., 2015). Up to DART 5.7.4, these images are generated by a bi-linear interpolation method.

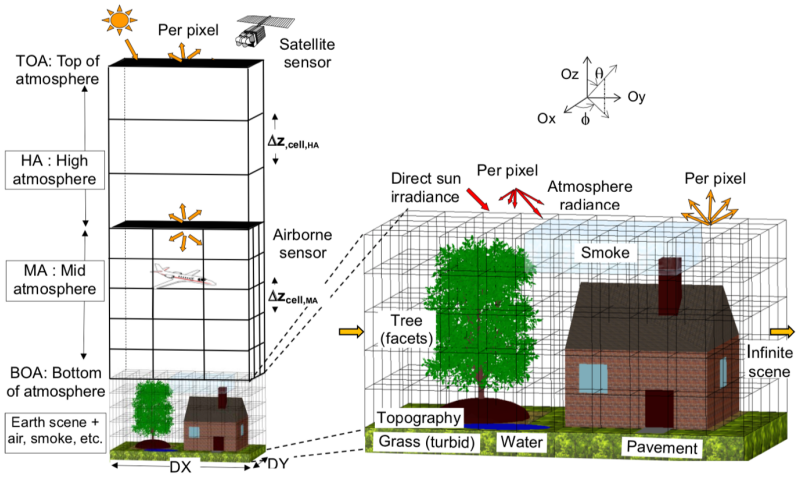

Figure 1. DART 3D discrete mock-up. Landscape elements are made of triangles, and/or fluid and turbid vegetation cells. The landscape itself is a cell matrix in order to ease ray tracing. The

atmosphere has three levels: upper level made of layers, middle level made of cells of any size, and lower level in the landscape.

DART simulates the RT in the Earth-atmosphere system with an iterative discrete ordinate method (Gastellu-Etchegorry et al. 1996, 2004, 2008, 2017), *i.e.*, radiation intercepted at iteration n is scattered at iteration $n + 1$, by tracking steady-state energy flux $W(r, \lambda, \Omega)$ (unit: W/sr/μm) along a finite number of directions Ω at position $r(x, y, z)$, at wavelength λ using the RT equation for a monochromatic radiation

$$\left(\xi \frac{d}{dx} + \eta \frac{d}{dy} + \mu \frac{d}{dz}\right) W(r, \lambda, \Omega) = -\alpha_e(r, \lambda, \Omega) W(r, \lambda, \Omega) + \alpha_a(r, \lambda, \Omega) W_B(T, \lambda, \Omega) + \int_0^{4\pi} \alpha_s(r, \lambda, \Omega') \frac{P(r, \lambda, \Omega' \rightarrow \Omega)}{4\pi} W(r, \lambda, \Omega') d\Omega' \quad (1)$$

where the term on the left side of equation (1) is the divergence of spectral energy, with (ξ, η, μ) being the unit vector of direction Ω. The three terms on the right side of equation (1) are the extinction and thermal emission along direction Ω, and the integrated scattering radiant flux into direction Ω over 4π space (Subrahmanyan Chandrasekhar, 2013). The total extinction coefficient α_e is the sum of absorption and scattering extinction coefficient ($\alpha_e = \alpha_a + \alpha_s$). W_B is the thermal energy flux emitted by a black body. $\frac{P(r,\lambda,\Omega' \rightarrow \Omega)}{4\pi}$ is the scattering phase function. It represents the proportion of incident flux along Ω' that is scattered per solid angle along Ω.

Figure 2 illustrates the 5 major steps of DART RT modelling in the Earth-atmosphere system. (1) Atmosphere thermal emission and sun illumination. (2) Earth surface RT. (3) Earth-

atmosphere radiative coupling. (4) Earth surface RT of atmosphere backscattered radiation. (5) Transfer of BOA upward radiation to any altitude, including TOA.

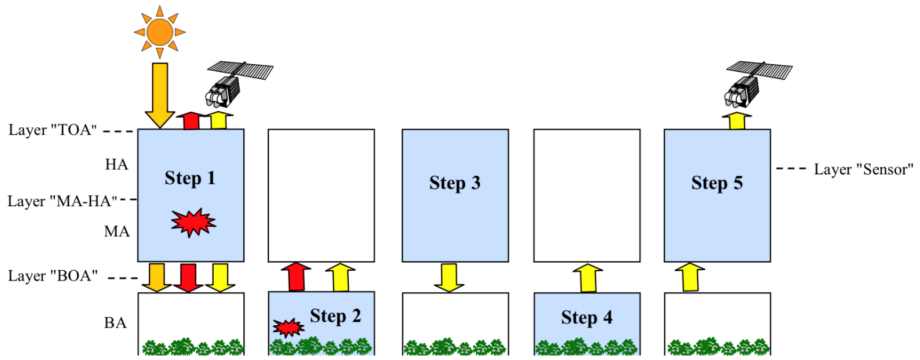

Figure 2. Major steps for modelling RT in the Earth-atmosphere system. Thermal emission in mode (T) is shown by the red symbol (steps 1 and 2). Arrows indicate directly transmitted solar (orange) and thermal (red) radiation, and scattered radiation (yellow), either thermal or solar.

2.2 Infinite slope mode

Earth surface RT is simulated with one of three modes. (1) Isolated scene mode (Figure 3.a). The Earth surface RT does not depend on neighbouring landscape: a ray that exits the scene does not re-enter the scene. It corresponds to laboratory experiments where only the studied scene is illuminated. (2) Repetitive scene mode (Figure 3.b). The landscape is an infinite horizontal duplication of the actually simulated scene: a ray that exits the 3D scene through a point M_{out} on a vertical face re-renters the scene along the same direction through a point M_{in} symmetric to M_{out}, at the same altitude. (3) Infinite slope mode (Figure 3.c). The landscape is an infinite duplication of the actually simulated scene with a continuity of slope and altitude at the DEM edges: a ray that exits the scene at M_{out} on a scene vertical face re-enters the scene at M_{in}, with an altitude shift equal to the altitude difference of the actually simulated scene and

the duplicated scene at ray exit face. The infinite slope mode was designed for the simulation of sloping landscapes. Conversely to the repetitive scene mode that leads to unrealistic border effects in presence of slope. Only the repetitive scene mode and the infinite slope mode can simulate environmental effect. Both verify the energy conservation.

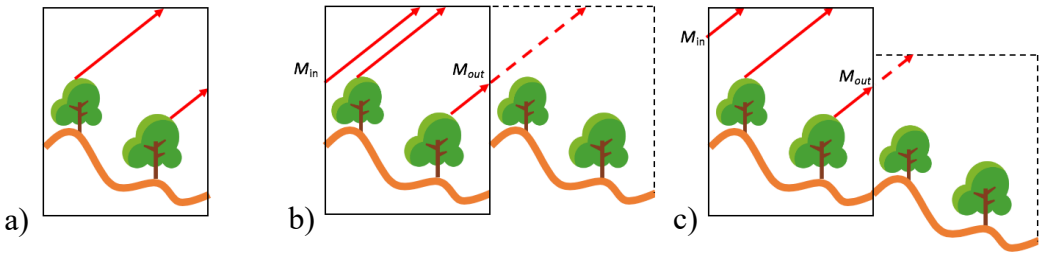

Figure 3. The three DART modes for simulating RT in 3D scenes. a) Isolated scene mode. b) Repetitive scene mode. c) Infinite slope mode. The actually simulated scene is framed by a black box. The dotted box frames one of the fictive neighbourhoods of the actually simulated scene.

2.3 Construction of infinite slope mock-up

In the infinite slope mode, the mean altitude of each edge of the DEM is computed to get the mean vertical shifts ΔZ_X and ΔZ_Y of the neighbour duplicated scenes, along the axes X and Y, respectively (Figure 4). Figure 4 displays the infinite spatial repetition of this Earth scene. If the altitudes of the opposite edges of a DEM are not parallel, the DEM edges and corners are smoothly connected by Bezier triangles (Gerald, 2014) to ensure the continuity of slopes and altitudes at the DEM edges of the actually simulated scene and its duplications. Whatever the Earth scene topography, the atmosphere above the BOA interface is horizontal, since density, pressure and temperature of DART atmosphere are assumed identical at the same altitude.

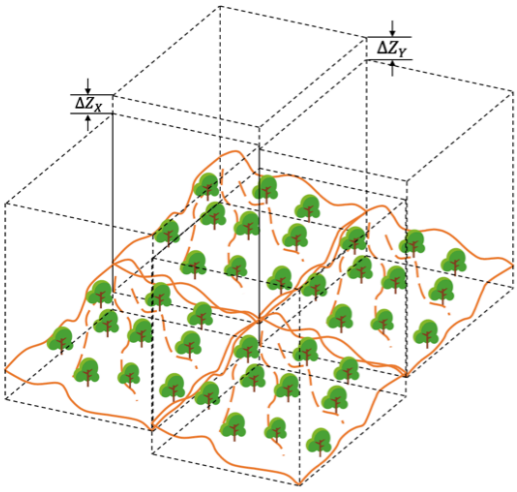

Figure 4. DART scene in infinite slope mode with its infinite duplications. Three duplications are shown here. The mean altitude differences between neighbour Earth scenes are indicated (ΔZ_X for axis X and ΔZ_Y for axis Y). DEM edges are smoothly connected with Bezier triangles.

3 Initial results and problems

3.1 Initial strategy

In the initial infinite slope mode, illumination (Figure 5.a) ray sources depart from the top scene and/or from a so-called "scene window". A scene window is the part of the scene vertical face through which an exit-ray will not re-enter the scene. Its spatial extent depends on the slope and ray direction. It is computed per illumination direction. Figure 5.a shows a simple 2D example with rays parallel to the paper plane. In 3D, the scene window geometry can be very complex to manage, which in turn can lead to serious illumination flaws. During the Earth surface RT modelling, a ray that exits the scene top/scene window along direction Ω_n is projected to the spread image on the Horizontal Plane (HP) (Figure 5.b), whereas a ray that crosses a scene vertical face outside the scene window re-enters the scene from the opposite face with an altitude shift (*i.e.*, ΔZ_X along axis X and ΔZ_Y along axis Y as indicated in Figure 4). The shape

and dimension of spread images on HP depend on the slope and ray direction. For some directions, the shape of spread images can be very complex polygons, possibly much larger than the scene horizontal section. The impossibility to accurately define their shapes for any configuration can introduce two other drawbacks. (1) Difficulty to connect the polygon-shape spread images to generate parallelogram shape image products. (2) Impossibility to know if pixels with zero value in the image plane corresponds to the spread image (*i.e.*, the observed scene), which can lead to images with overestimated mean radiance if totally shadowed zones are observed (*i.e.*, apparent reflectance equal to zero).

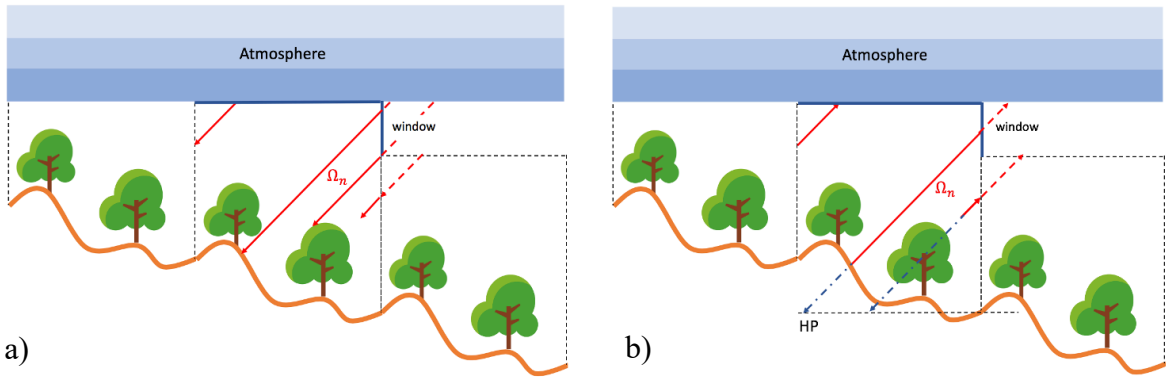

Figure 5. 2D view of the infinite slope mode RT modelling of initial DART. a) Illumination stage. b) Spread image generation stage. The scene window for direction Ω_n is the dark blue region at the scene vertical face. Its shape depends on the DEM and the illumination direction. Red arrows are rays in the paper plane. Illumination ray sources start from the scene top and window. Rays that cross scene top/window never re-enter the scene, conversely to rays that cross other parts of the scene vertical face. HP is the horizontal plane that stores the spread images.

Atmosphere backscattered energy and RS images are derived from spread images on HP. In the Earth-Atmosphere coupling stage, upward rays are assumed to come from the rectangular scene top, since the shape of spread images is too complex to manage. In the RS image generation

stage, the centre of each sensor pixel (i, j) is projected onto HP along its viewing direction, Figure 6.a illustrates a pinhole camera image generation process. Then, a bi-linear interpolation method derives the pixel value $X_{\text{sensor}}(i,j)$ from the values of four pixels ($X_{\text{HP}}(i',j')$, $X_{\text{HP}}(i'+1,j')$, $X_{\text{HP}}(i',j'+1)$, $X_{\text{HP}}(i'+1,j'+1)$) on HP that surround the projected point (Eq. (2)).

$$X_{\text{sensor}}(i,j) = (X_{\text{HP}}(i',j') \cdot \Delta x_1 + X_{\text{HP}}(i'+1,j') \cdot \Delta x_2) \cdot \Delta y_1 + (X_{\text{HP}}(i',j'+1) \cdot \Delta x_1 + X_{\text{HP}}(i'+1,j'+1) \cdot \Delta x_2) \cdot \Delta y_2 \quad (2)$$

where Δx and Δy are the scale coefficients between 0 and 1, they are shown in Figure 6.b.

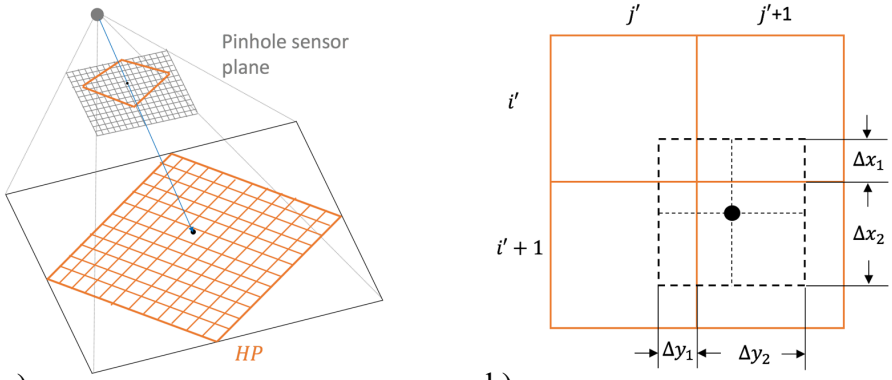

Figure 6. Pinhole camera image generation using an interpolation method. a) Projection onto HP of the centre of a pixel in the sensor image. b) Nadir view of the projected point. Δx and Δy are the scale coefficients that vary from 0 to 1.

3.2 Results and problems

This section illustrates issues of the initial infinite slope mode through visual and statistical analysis of DART BRF profile, and RB and RS images (Figure 7 and Figure 8). To facilitate the analysis, two solo slope simulations are analysed, first a slope with a Lambertian bare ground (Figure 7.a), and then a slope with a tree (Figure 8.a). Table 2 lists DART input parameters. The solo slope is created by the DART DEM generator. Figure 7.b shows its energy

map (*i.e.*, intercepted flux $\sum_z W(i,j,z)$ (W/µm) per pixel (i,j)) with regular microgrooves and polygon-shapes. The intercepted energy flux has a relative variability $(W_{\max}\text{-}W_{\min})/W_{\text{mean}}$ up to 25% although it should be zero. It is due to a mismanagement of illumination and coupling energy. Figure 7.c shows the scene reflectance in the solar plane, the BRF varies up to 11% relative to nadir reflectance whereas it should be a constant. Its dependence on the viewing zenith angle θ_v is due to the boarder effect when connecting polygon-shape spread images. It is all the more serious if the viewing direction is close to the slope (viewing zenith angle $\theta_v < -54°$ in Figure 7.c).

The simulation of a cherry tree on the solo slope illustrates other issues. Tree trunk, branches and leaves are Lambertian surfaces. Figure 8.b-f shows DART RS images: satellite (orthographic) camera for viewing directions equal to ($\theta_{\text{sensor}}=41°$, $\varphi_{\text{sensor}}=194°$) (b) and ($\theta_{\text{sensor}}=80°$, $\varphi_{\text{sensor}}=355°$) (c), fisheye camera (d), pinhole camera (e) and pushbroom (f). Several issues affect image quality: (1) microgrooves, (2) border effect, and (3) erroneous areas. Microgrooves arise because the ray illumination mesh on the object surface is coarser than DART cell dimensions, for some directions. As a result, triangles between two rays are less illuminated. If the image resolution is high enough, these less illuminated triangles can lead to lines of darker pixels. Because of the microgrooves, the reflectance of ground (averagely 0.29) in Figure 8.b has maximum difference 0.04 with standard deviation 0.004. The initial modelling strategy did not manage the spatial variability of the density of illumination rays on local topography. Hence, the density of illumination rays varies with the local slopes, although it is spatially uniform on the BOA horizontal plane. The second and third issues arise with the procedure that connects the spread images. In the initial strategy, the polygon-shape spread images are juxtaposed in order to obtain a parallelogram RS image. According to the definition of the infinite slope, the opposite sides of any spread image should be continuous. However,

297 this is not always the case if the slope or the viewing direction is very oblique. Also,
298 discretization explains that pixel values on the borders of a spread image can be over or
299 underestimated. It results that the connected borders of the spread image appear with darkish
300 and whitish tones in the final image (Figure 8.b). The complex shape of the spread images also
301 gives rise to zones without signal (*i.e.*, yellow zones) or with overestimated neighbour zones
302 (*i.e.*, whitish zones) (Figure 8.c). In addition, the yellow zone on the cherry tree in Figure 8.c
303 has zero reflectance. These zones are discarded since the initial algorithm cannot distinguish
304 zero radiance and no-signal pixel.
305
306 In short, Figure 7 and Figure 8 stress two major sources of inaccuracy of the initial infinite
307 slope mode: scene illumination and polygon-shape spread image management. An important
308 technical drawback must be noted as well: the required RAM to store images greatly increases
309 with the obliquity of viewing directions. For example, in the above schematic example, the
310 infinite slope mode requires more than 8 times RAM than the repetitive scene mode. The next
311 section presents a new modelling strategy that was developed to improve this situation.
312
313 Table 2. DART input parameters. θ is a zenith angle, φ is an azimuth angle oriented anticlockwise
314 from South ($\varphi_{\text{South}} = 0°$, $\varphi_{\text{East}} = 90°$, $\varphi_{\text{North}} = 180°$ and $\varphi_{\text{West}} = 270°$). ρ is a reflectance.
315 Dash symbol stands for "no-value". USSTD76 atmospheric constituent profile and RURAL
316 aerosol model are defined in Anderson et al., 1986 and Shettle and Fenn, 1979, respectively.

Parameters	Solo slope	Solo slope + Cherry tree
Spectral band	0.56 μm	0.56 μm
Sun direction	θ_{sun}=30°, φ_{sun}=225°	θ_{sun}=30°, φ_{sun}=225°
Atmosphere model	USSTD76	USSTD76

Aerosol model	RURAL_V23KM	RURAL_V23KM
Scene dimension	X = Y = 40 m	X = Y = 40 m
Spatial resolution	0.125 m	0.125 m
DEM	30° solo slope (φ_{slope}=45°)	30° solo slope (φ_{slope}=45°)
ρ_{ground}	0.5	0.5
Tree	-	Cherry tree
Tree position	-	$x = y = 20$ m
ρ_{leaf}	-	0.11
τ_{leaf}	-	0.1
ρ_{trunk}	-	0.075

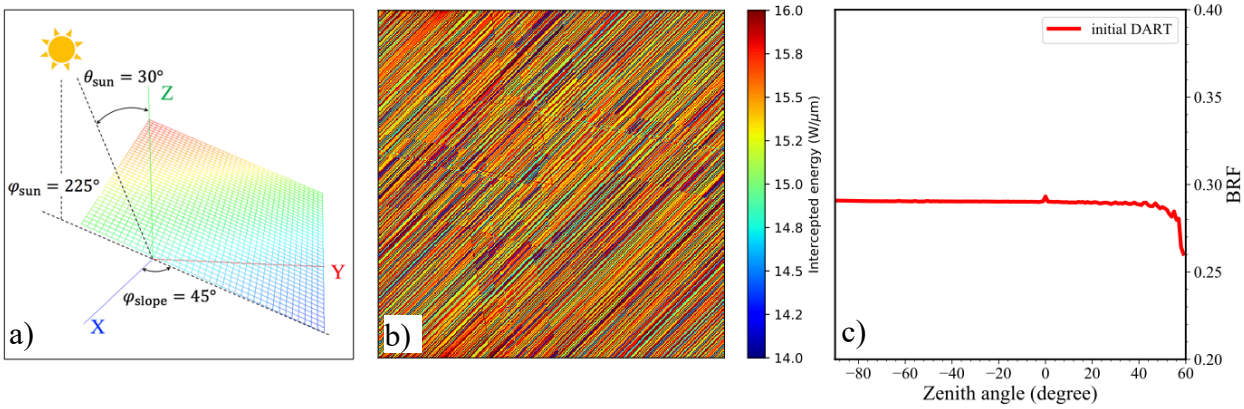

Figure 7. Simulation of a solo slope, using the initial infinite slope mode. DEM mesh with indication of slope azimuth angle φ_{slope}, and zenith and azimuth angles (θ_{sun}, φ_{sun}) of the direction in which the sun is seen from the Earth surface (a), φ is anticlockwise from South. Solo slope: spectral energy flux map (b) and angular reflectance in the solar plane (c).

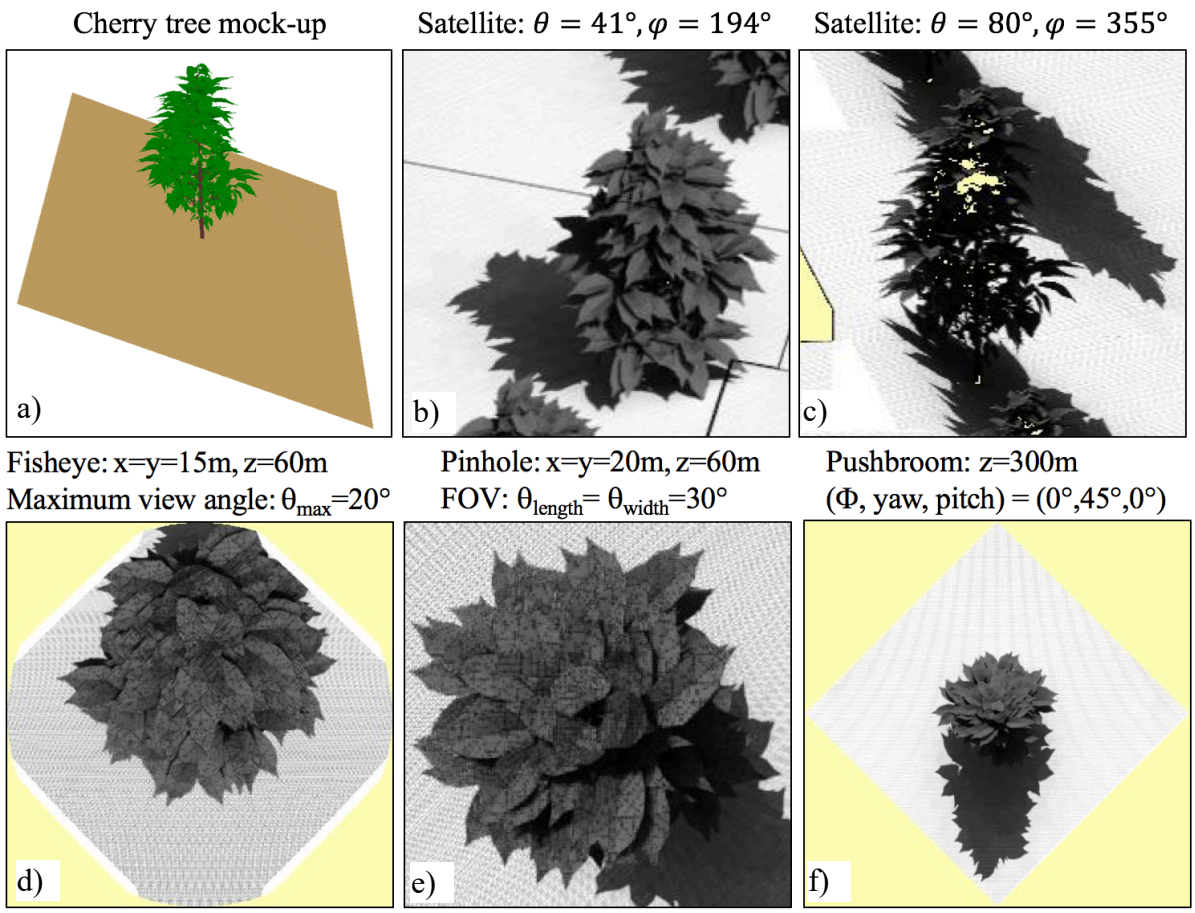

Figure 8. Simulation of a cherry tree on a solo slope, using the initial infinite slope mode. Satellite (orthographic) camera images (b, c) with 2 viewing directions, fisheye camera image (d), pinhole camera image (e) and pushbroom image (f).

4 The new infinite slope mode

4.1 Introduction of oblique planes OP

The new modelling strategy of the infinite slope mode aims to get more accurate and more systematic modelling of the scene illumination, the Earth-atmosphere radiative coupling, and the image generation, for sloping landscapes. The innovation is to introduce an auxiliary oblique plane OP that depends only on topography to store spread images and to simulate scene

illumination, instead of HP. OP ensures that the spread images have the same shape and size, and that the RAM demand is independent of topography. Geometrically, OP is a parallelogram, the four sides of which belong to the four vertical faces of the scene (Figure 9.b). The opposite sides of OP have altitude differences ΔZ_X along axis X and ΔZ_Y along axis Y equal to the altitude differences between the duplicated scenes (Figure 4, Figure 9.b). The vertical projection of any OP pixel on HP has the same size and shape as DART scene cells.

DART atmospheric RT and Earth surface RT modelling are sequential. In the scene illumination and Earth-atmosphere radiative coupling stages, energy conservation is ensured. To quantify downward radiation from the horizontal atmosphere to OP and upward radiation from OP to the horizontal atmosphere, the parallel projection of OP along Ω_n onto a horizontal plane is computed per direction Ω_n. Its projected surface $\Sigma_p(\Omega_n)$ (Figure 9.c) is a parallelogram. The four corner coordinates (x_p, y_p, z_p) of $\Sigma_p(\Omega_n)$ depend on the direction vector Ω_n and the coordinates (x_o, y_o, z_o) of the four corners of OP. Ω_n is characterized by its zenith angle θ and azimuth angle φ. We have $\theta = 0°$ for nadir direction, ($\theta = 90°$, $\varphi = 0°$) for a direction parallel to the x-axis, and ($\theta = 90°$, $\varphi = 90°$) for a direction parallel to the y-axis.

$$\begin{cases} z_p - z_o = d\cos\theta \\ x_p - x_o = d\sin\theta\cos\varphi \\ y_p - y_o = d\sin\theta\sin\varphi \end{cases} \quad (3)$$

where d is the distance between OP corner (x_o, y_o, z_o) and the projected point (x_p, y_p, z_p). The norm of the cross product of any two adjacent sides of the projected parallelogram $\Sigma_p(\Omega_n)$ is its area $S_p(\Omega_n)$. Note that the parallel projection of OP on any horizontal plane, including the horizontal atmosphere, gives the same projected area $S_p(\Omega_n)$.

In presence of slope, if the viewing direction is more inclined than the slope (*i.e.*, $\Omega_n^{\uparrow} \cdot \boldsymbol{n} < 0$, with $\boldsymbol{n}$ the normal of OP), no signals can be observed along these upward directions $\Omega_n^{\uparrow}$. In addition, if the illumination direction is more inclined than the slope (*i.e.*, $\Omega_n^{\downarrow} \cdot \boldsymbol{n} > 0$), no light along these downward directions $\Omega_n^{\downarrow}$ can reach the scene. Therefore, these directions are set as inactive and called inactive directions $\Omega_{n,\text{inactive}}$. Inactive downward directions $\Omega_{n,\text{inactive}}^{\downarrow}$ are eliminated during the illumination stage, and inactive upward directions $\Omega_{n,\text{inactive}}^{\uparrow}$ are not considered to compute atmosphere backscattered energies.

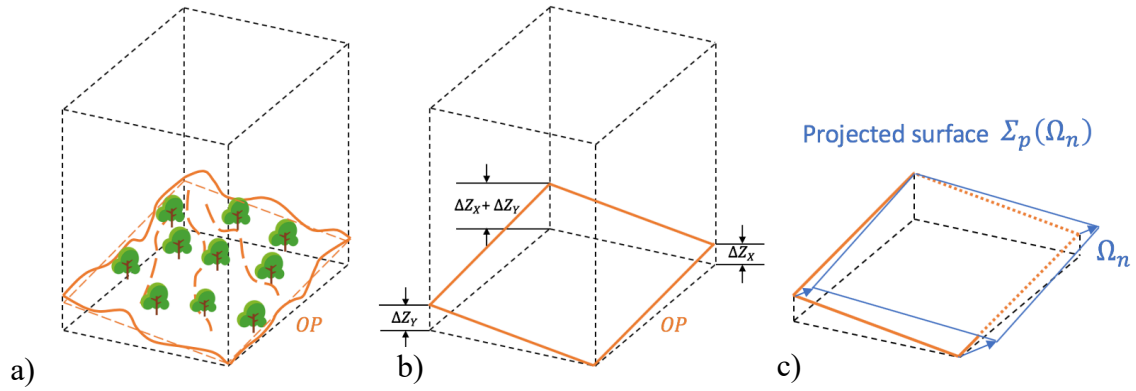

Figure 9. DART infinite slope mode. a) Earth scene and its fictive oblique plane OP at the scene bottom. b) DEM altitude differences are ΔZ_X along axis X and ΔZ_Y along axis Y axis. c) Projected surface (blue parallelogram) $\Sigma_p(\Omega_n)$ of OP along direction Ω_n onto the horizontal plane that contains the highest point of OP, it has an area equal to $S_p(\Omega_n)$.

4.2 Illumination of the Earth scene

Atmospheric RT modelling, including sun radiation and atmosphere thermal emission and scattering, gives a spectral energy flux $W_h(\Omega_n)$ [W/µm] per direction $(\Omega_n, \Delta\Omega_n)$ per spectral band in three fictive layers (Gastellu-Etchegorry et al., 1996). (1) BOA: $W_{\text{BOA}}(\Omega_n^{\downarrow})$ [W/µm]

per downward direction $\Omega_n^{\downarrow}$ including solar direction Ω_s. (2) TOA: $W_{\mathrm{TOA}}(\Omega_n^{\uparrow})$ [W/μm] per upward direction $\Omega_n^{\uparrow}$. (3) Sensor layer at any altitude h: $W_{\mathrm{sensor}}(\Omega_n)$ [W/μm] per upward and downward direction Ω_n. Equation (4) gives the irradiance of each fictive layer.

$$E_{\mathrm{BOA}}^{\mathrm{dir}} = \frac{W_{\mathrm{BOA}}(\Omega_s)}{S_{\mathrm{scene}}}, \qquad E_{\mathrm{BOA}}^{\mathrm{diff}} = \frac{\sum_{\Omega_n^{\downarrow}} W_{\mathrm{BOA}}(\Omega_n^{\downarrow})}{S_{\mathrm{scene}}}$$
$$E_{\mathrm{sensor}}^{\mathrm{dir}} = \frac{W_{\mathrm{sensor}}(\Omega_s)}{S_{\mathrm{scene}}}, \qquad E_{\mathrm{sensor}}^{\mathrm{diff}} = \frac{\sum_{\Omega_n^{\downarrow}} W_{\mathrm{sensor}}(\Omega_n^{\downarrow})}{S_{\mathrm{scene}}} \tag{4}$$

with S_{scene} the area of scene horizontal section, E^{dir} the direct irradiance and E^{diff} the diffused irradiance.

The downward flux incident along direction $\Omega_n^{\downarrow}$ on a pixel (i, j) at BOA level, knowing that the BOA interface has $I_{\mathrm{BOA}} \cdot J_{\mathrm{BOA}}$ pixels, is

$$W_{\mathrm{BOA}}(i, j, \Omega_n^{\downarrow}) = \frac{W_{\mathrm{BOA}}(\Omega_n^{\downarrow})}{I_{\mathrm{BOA}} \cdot J_{\mathrm{BOA}}} \tag{5}$$

Using the law of conservation of energy, the incident energy flux per direction $\Omega_n^{\downarrow}$ on pixel (i, j) of OP (*i.e.*, I_{BOA} lines and J_{BOA} columns) is

$$W_{\mathrm{OP}}(i, j, \Omega_n^{\downarrow}) = W_{\mathrm{BOA}}(i, j, \Omega_n^{\downarrow}) \cdot \frac{S_p(\Omega_n^{\downarrow})}{S_{\mathrm{scene}}} \tag{6}$$

with $S_p(\Omega_n^{\downarrow})$ the projected surface of OP onto the horizontal atmosphere along direction $\Omega_n^{\downarrow}$.

In the illumination stage, M equal energy rays are sent per OP pixel per downward direction to illuminate the Earth scene. To uniformly illuminate sloping terrains (*i.e.*, same user-defined ray density M per direction), the illumination position $P_{\mathrm{OP}}(x, y, z)$ on OP is first sampled using a semi-random method per pixel (i, j). Note a larger M improves the accuracy of results but increases computation time. Default $M = 100$ is a compromise between accuracy and time cost.

Then, $P_{\mathrm{OP}}(x,y,z)$ is projected to the scene top and scene window per downward direction $\Omega_n^{\downarrow}$ with a backward ray tracing method to set the ray source position $P_{\mathrm{ray}}(x,y,z)$ (Figure 10) at scene top or scene window. Ray energy flux $W_{\mathrm{ray}}\left(i,j,\Omega_n^{\downarrow},P_{\mathrm{ray}}\right)$ is computed only for active directions.

$$W_{\mathrm{ray}}\left(i,j,\Omega_n^{\downarrow},P_{\mathrm{ray}}\right)=\frac{W_{\mathrm{OP}}\left(i,j,\Omega_n^{\downarrow}\right)}{M} \tag{7}$$

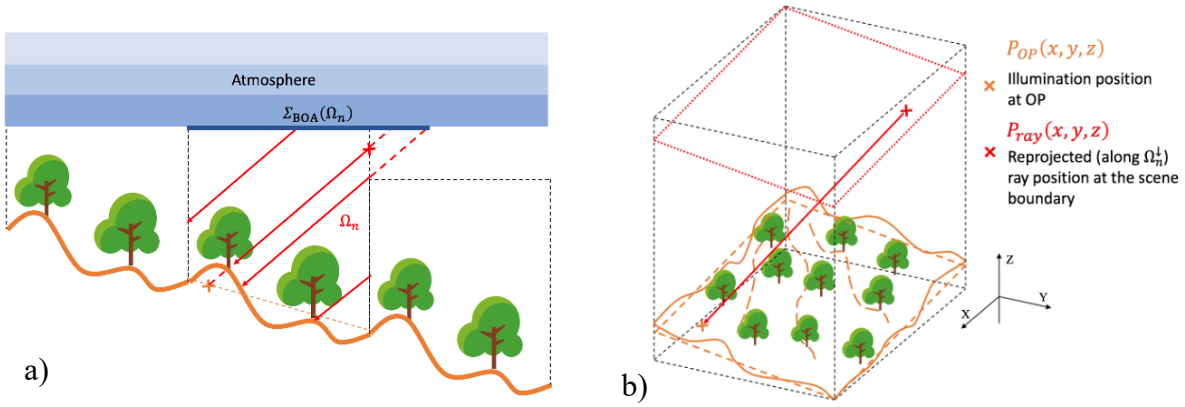

Figure 10. 2D (a) and 3D (b) views of the scene illumination stage. $\Sigma_{\mathrm{BOA}}(\Omega_n)$ is the projected surface of OP onto the horizontal BOA plane with backward ray tracing method; its area is $S_p(\Omega_n)$. After atmospheric RT modelling, rays through $\Sigma_{\mathrm{BOA}}(\Omega_n)$ along direction Ω_n illuminates the scene. $P_{\mathrm{ray}}(x,y,z)$ (x) is the source point of an incident ray, on the scene top or scene window. $P_{\mathrm{OP}}(x,y,z)$ (x) is the projection on OP of $P_{\mathrm{ray}}(x,y,z)$ along incident direction Ω_n.

4.3 Spread of ray energy on OP during Earth surface RT modelling

After the illumination and landscape thermal emission stages, the scene surface and volume elements iteratively scatter all or part of the intercepted radiation, *i.e.*, radiation intercepted at iteration n is scattered at iteration $n+1$ (*i.e.*, step 2 in Figure 2). The number of iterations must

be large enough in order to get accurate results. It depends on the spectral domain and on landscape characteristics. Generally, the energy flux cumulated on the spread images follows an exponential relation with iteration number n (Kallel Abdelaziz, 2018). Hence, at the end of the Earth surface RT process, the energy fluxes per pixel per direction $W^{\text{iter } n}\left(i,j,\Omega_n^{\uparrow}\right)$ at different iteration orders n are extrapolated to get $W^{\text{iter } X}\left(i,j,\Omega_n^{\uparrow}\right)$ at an infinite iteration order. Upward radiation that exits the scene top/window is projected onto OP (Figure 11.a) at the scene bottom along its propagation direction instead of HP at scene bottom (Figure 5.b) as in the original DART RT modelling in Gastellu-Etchegorry et al., 1996. Storing ray energy in a plane at the bottom of the scene minimizes the shift of Earth objects in directional images and simplifies the generation of RS images (Yin et al., 2015).

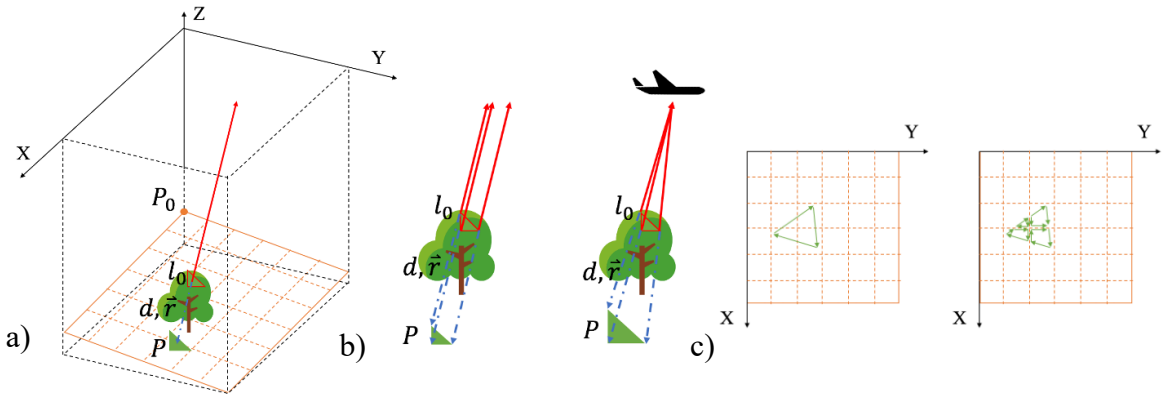

Figure 11. Ray projection on OP. a) The red triangle gives rise to a ray along direction $\boldsymbol{r}$ (red arrow) that reaches the scene top. The green triangle is its projection onto OP. P is the projection on OP of a corner l_0 of the red triangle. d is the distance $\|P - l_0\|$. P_0 is the highest point of OP. b) Parallel projection for the orthographic camera and perspective projection for the perspective camera. c) Nadir view of the projected triangle on OP and its break-down into four polygons.

The projection process is presented here. Let a facet Σ in the 3D scene gives rise to an emitted and/or scattered energy flux along direction $\boldsymbol{r}$ that exits the scene top or scene window. In that case, Σ is projected along $\boldsymbol{r}$ onto OP where the energy flux is stored per pixel in a spread image. Its projected surface is Σ_{OP} (Figure 11.a). Let a corner P of Σ_{OP} be the projection of a corner l_0 of Σ along direction $\boldsymbol{r}$ onto OP (normal $\boldsymbol{n}$) (Figure 11.a), P_0 the highest point of OP, and d the distance $\|P - l_0\|$. The coordinate of P is computed with

$$\begin{cases} (P_0 - P) \cdot \boldsymbol{n} = 0 \\ P = l_0 + d \cdot \boldsymbol{r} \end{cases} \Rightarrow \begin{cases} d = \dfrac{(P_0 - l_0) \cdot \boldsymbol{n}}{\boldsymbol{r} \cdot \boldsymbol{n}} \\ P = l_0 + d \cdot \boldsymbol{r} \end{cases} \tag{8}$$

In Figure 11.c, the projected surface Σ_{OP} is at the intersection of four pixels. Hence, it is partitioned into four polygons with one polygon Σ_{OP}^{k} per pixel k. The energy flux distributed per pixel k is proportional to the surface ratio $\Sigma_{\mathrm{OP}}^{k}/\Sigma_{\mathrm{OP}}$.

After the Earth surface RT stage, DART products (reflectance $\rho^{\mathrm{iterX}}\left(i,j,\Omega_n^{\uparrow}\right)$, radiance $L^{\mathrm{iterX}}\left(i,j,\Omega_n^{\uparrow}\right)$, brightness temperature $T_B^{\mathrm{iterX}}\left(i,j,\Omega_n^{\uparrow}\right)$, etc.) and their mean values are derived (Eq. (9)) from the energy fluxes $W_{\mathrm{OP}}^{\mathrm{iterX}}\left(i,j,\Omega_n^{\uparrow}\right)$ per pixel per direction on the spread images.

$$\begin{gathered} L^{\mathrm{iterX}}\left(i,j,\Omega_n^{\uparrow}\right) = \frac{W_{\mathrm{OP}}^{\mathrm{iter\,X}}\left(i,j,\Omega_n^{\uparrow}\right)}{S_p\left(i,j,\Omega_n^{\uparrow}\right)\cdot\cos\theta_n\cdot\Delta\Omega_n^{\uparrow}},\ \rho^{\mathrm{iterX}}\left(i,j,\Omega_n^{\uparrow}\right) = \frac{\pi\cdot L^{\mathrm{iter\,X}}\left(i,j,\Omega_n^{\uparrow}\right)}{E_{\mathrm{BOA}}^{\mathrm{dir}}+E_{\mathrm{BOA}}^{\mathrm{diff}}}, \\ \bar{L}^{\mathrm{iter\,X}}\left(\Omega_n^{\uparrow}\right) = \frac{\sum_i\sum_j L^{\mathrm{iter\,X}}\left(i,j,\Omega_n^{\uparrow}\right)}{I_{\mathrm{BOA}}\cdot J_{\mathrm{BOA}}},\ \omega_{\mathrm{scene}}^{\mathrm{iter\,X}} = \frac{\sum_{\Omega_n^{\uparrow}} \bar{L}^{\mathrm{iter\,X}}\left(\Omega_n^{\uparrow}\right)\cos\theta_n\Delta\Omega_n^{\uparrow}}{E_{\mathrm{BOA}}^{\mathrm{dir}}+E_{\mathrm{BOA}}^{\mathrm{diff}}} \end{gathered} \tag{9}$$

with $S_p\left(i,j,\Omega_n^{\uparrow}\right)$ the projected surface of OP pixel (i,j) onto HP along direction $\Omega_n^{\uparrow}$, $\Delta\Omega_n^{\uparrow}$ the solid angle of direction $\Omega_n^{\uparrow}$, and θ_n the zenith angle of direction $\Omega_n^{\uparrow}$. $\bar{L}\left(\Omega_n^{\uparrow}\right)$ is the average exitant radiance along direction $\Omega_n^{\uparrow}$ and ω_{scene} is the scene albedo.

4.4 Earth surface RT of the atmosphere backscattered radiation

After the Earth surface RT stage (*i.e.*, step 2 in Figure 2), part of the upward flux $W_{\mathrm{OP}}^{\mathrm{iter\,X}}\left(i,j,\Omega_n^{\uparrow}\right)$ that exits the scene is backscattered by the atmosphere to the Earth surface (*i.e.*, step 3 in Figure 2). The backscattered flux is computed by convolving upward radiation from the Earth scene with transfer function $\mathrm{TF}_{\mathrm{BA-BA}}(\Omega_n^{\uparrow},\Omega_n^{\downarrow})$ (Grau and Gatellu-Etchegorry, 2013)

$$W_{\mathrm{BOA}}^{\mathrm{backscat}}\left(\Omega_n^{\downarrow}\right)=\frac{1}{1\text{ - }\omega_{\mathrm{scene}}\cdot\bar{S}}\sum\nolimits_{\Omega_n^{\uparrow}}W_{\mathrm{BOA}}^{\mathrm{iter\,X}}(\Omega_n^{\uparrow})\cdot\mathrm{TF}_{\mathrm{BA-BA}}(\Omega_n^{\uparrow},\Omega_n^{\downarrow}) \tag{10}$$

with $\bar{S}$ the average atmosphere albedo and $W_{\mathrm{BOA}}^{\mathrm{iter\,X}}\left(\Omega_n^{\uparrow}\right)=\sum_i\sum_j W_{\mathrm{OP}}^{\mathrm{iter\,X}}\left(i,j,\Omega_n^{\uparrow}\right)\cdot\frac{S_{\mathrm{scene}}}{S_p(\Omega_n^{\uparrow})}$ the upward energy flux at BOA along direction $\Omega_n^{\uparrow}$. $W_{\mathrm{BOA}}^{\mathrm{backscat}}\left(\Omega_n^{\downarrow}\right)$ is used to get backscattered energy flux per pixel per direction at BOA $W_{\mathrm{BOA}}^{\mathrm{backscat}}\left(i,j,\Omega_n^{\downarrow}\right)=\frac{W_{\mathrm{BOA}}^{\mathrm{backscat}}(\Omega_n^{\downarrow})}{I_{\mathrm{BOA}}\cdot J_{\mathrm{BOA}}}$ and the atmosphere backscattered irradiance $E_{\mathrm{BOA}}^{\mathrm{backscat}}=\frac{\sum_{\Omega_n^{\downarrow}}W_{\mathrm{BOA}}^{\mathrm{backscat}}(\Omega_n^{\downarrow})}{S_{\mathrm{scene}}}$. More Details are given in appendix A.

Atmosphere backscattering gives a new Earth scene illumination (*i.e.*, step 4 in Figure 2). The resulting backscattered flux per OP pixel (Eq. (11)) ensures the conservation of energy (Eq. (6))

$$W_{\mathrm{OP}}^{\mathrm{backscat}}\left(i,j,\Omega_n^{\downarrow}\right)=W_{\mathrm{BOA}}^{\mathrm{backscat}}\left(i,j,\Omega_n^{\downarrow}\right)\cdot\frac{S_p\left(\Omega_n^{\downarrow}\right)}{S_{\mathrm{scene}}} \tag{11}$$

Then, the Earth surface RT is simulated again, and upward energy $W_{\mathrm{OP}}(i,j,\Omega_n^{\uparrow})$ per direction is cumulated per OP pixel per direction. The resulting upward flux $W_{\mathrm{OP}}^{\mathrm{coupl}}(i,j,\Omega_n^{\uparrow})$ is used to compute pixel and scene radiance and reflectance products (marked as coupl in equation (12)).

$$L^{\mathrm{coupl}}\left(i,j,\Omega_n^{\uparrow}\right)=\frac{W_{\mathrm{OP}}^{\mathrm{coupl}}(i,j,\Omega_n^{\uparrow})}{S_p(i,j,\Omega_n^{\uparrow})\cdot\cos\theta_n\cdot\Delta\Omega_n^{\uparrow}},\ \rho^{\mathrm{coupl}}\left(i,j,\Omega_n^{\uparrow}\right)=\frac{\pi\cdot L^{\mathrm{coupl}}(i,j,\Omega_n^{\uparrow})}{E_{\mathrm{BOA}}^{\mathrm{dir}}+E_{\mathrm{BOA}}^{\mathrm{diff}}+E_{\mathrm{BOA}}^{\mathrm{backscat}}} \tag{12}$$

$$\bar{L}^{\text{coupl}}\left(\Omega_n^{\uparrow}\right)=\frac{\sum_i \sum_j L^{\text{coupl}}(i,j,\Omega_n^{\uparrow})}{I_{\text{BOA}} \cdot J_{\text{BOA}}},\ \omega_{\text{scene}}^{\text{coupl}}=\frac{\sum_{\Omega_n^{\uparrow}} \bar{L}^{\text{coupl}}(\Omega_n^{\uparrow}) \cos\theta_n \Delta\Omega_n^{\uparrow}}{E_{\text{BOA}}^{\text{dir}}+E_{\text{BOA}}^{\text{diff}}+E_{\text{BOA}}^{\text{backscat}}}$$

462 Fluxes $W_{\text{OP}}^{\text{coupl}}(i,j,\Omega_n^{\uparrow})$ are tracked in the atmosphere and then cumulated at TOA and sensor
463 levels (*i.e.*, step 5 in Figure 2) (Grau and Gatellu-Etchegorry, 2013). More details are given in
464 appendix B.
465

466 **4.5 Image generation**

467

468 Once the radiometric products are computed as spread images, they are projected to the sensor
469 plane. Here, the initial algorithm (Gastellu-Etchegorry et al., 2008; Yin et al., 2015) is improved
470 to get more accurate sensor images: sensor image pixel value is computed with a precise
471 projection method instead of the bi-linear interpolation method. In addition, the lambert
472 azimuthal equal-area projection is introduced to generate fisheye images.
473

474 Although the interpolation method is simple to implement and computer efficient, it degrades
475 images, and the associated error increases for sloping landscapes and oblique viewing directions.
476 Hence, we implemented a precise projection method that costs reasonable calculation time. For
477 satellite (orthographic) camera, spread image pixels are parallelly projected to sensor plane
478 along the viewing direction Ω_n (Figure 12.a). For pinhole and pushbroom camera, spread image
479 pixels are perspectively projected to sensor plane along the local viewing direction Ω_n to
480 camera focus (Figure 12.b, c). For fisheye camera, pixels are projected to a unit sphere along
481 its local viewing direction to the camera focus and then this pixel on the unit sphere is spread
482 on the image plane at the bottom of the unit sphere using the Lambert azimuthal equal-area
483 projection equation (Eq. (13)) that projects any point (x,y,z) on the unit sphere onto its bottom
484 plane at $(X,Y,-1)$ (Figure 13).

$$(X, Y, Z) = \left(\sqrt{\frac{2}{1-z}}\, x, \sqrt{\frac{2}{1-z}}\, y, -1 \right) \tag{13}$$

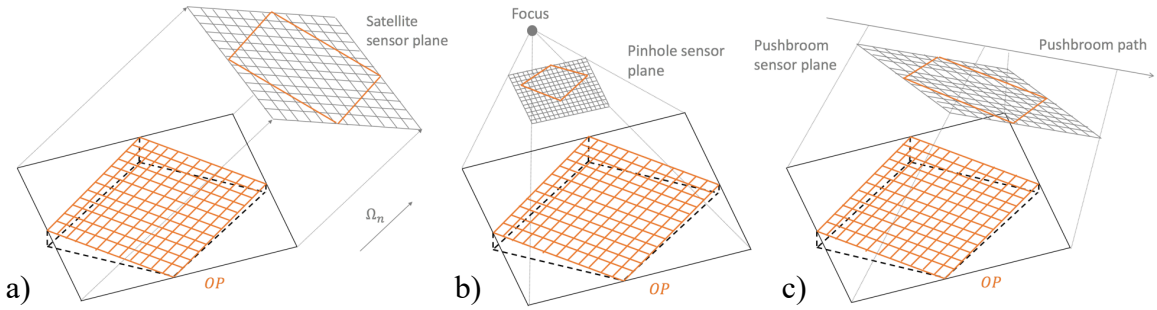

Figure 12. Projection processes for simulating images. Parallel projection along direction Ω_n for satellite (orthographic) camera (a), and perspective projection along local viewing direction for pinhole camera (b) and pushbroom camera (c).

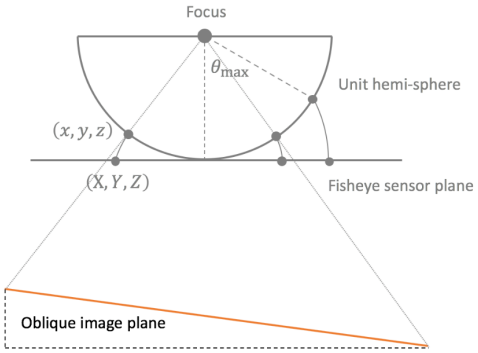

Figure 13. Projection processes for simulating fisheye images. First, pixel on OP is projected onto a unit sphere. Then, it is spread on the sensor plane with Lambert azimuthal equal-area projection method that projects a point (x, y, z) of the unit sphere onto the sensor plane at point (X, Y, Z). $\theta_{\max}$ is the maximum viewing zenith angle.

Image dimensions, resolutions and field of view (FOV) are user-defined for perspective and fisheye cameras whereas image resolution is that of DART cell dimensions for satellite (orthographic) cameras. Projected images are further rasterized by the pixel grid in the sensor plane. For that, the four corners of each pixel (i', j') on OP are projected to the sensor plane along the viewing direction $\Omega_n^{\uparrow}$, where they make up a new quadrilateral $\Sigma_{i',j'}^{\text{sensor}}$. As in section 4.3, $\Sigma_{i',j'}^{\text{sensor}}$ is spread over sensor pixels, and $f(i, j, i', j', \Omega_n^{\uparrow})$ stores the part of $\Sigma_{i',j'}^{\text{sensor}}$ in a sensor pixel (i, j). For example, $f\left(i, j, i', j', \Omega_n^{\uparrow}\right) = 0.5$ if $\Sigma_{i',j'}^{\text{sensor}}$ occupies 50% surface of a sensor pixel (i, j). For any radiometric product, sensor pixel values $X_{\text{sensor}}\left(i, j, \Omega_n^{\uparrow}\right)$ are resampled (Eq. (14)) using the values $X_{\text{OP}}\left(i', j', \Omega_n^{\uparrow}\right)$ of the projected OP pixels.

$$X_{\text{sensor}}\left(i, j, \Omega_n^{\uparrow}\right) = \sum_{i'} \sum_{j'} X_{\text{OP}}\left(i', j', \Omega_n^{\uparrow}\right) \cdot f\left(i, j, i', j', \Omega_n^{\uparrow}\right) \tag{14}$$

Coordinates $(x_{\text{DART}}, y_{\text{DART}}, z_{\text{DART}})$ in the scene reference are transformed into coordinates $(x_{\text{sensor}}, y_{\text{sensor}}, z_{\text{sensor}})$ in the sensor reference with a transfer matrix A (Eq. (15)), where $(\theta, \varphi) = \text{sensor}(\text{zenith}, \text{azimuth})$ angles in the DART scene coordinate reference.

$$\begin{bmatrix} x_{\text{sensor}} \\ y_{\text{sensor}} \\ z_{\text{sensor}} \end{bmatrix} = \text{A} \begin{bmatrix} x_{\text{DART}} \\ y_{\text{DART}} \\ z_{\text{DART}} \end{bmatrix} \quad \text{with A} = \begin{bmatrix} \cos\theta\cos\varphi & \cos\theta\sin\varphi & -\sin\theta \\ -\sin\varphi & \cos\varphi & 0 \\ \sin\theta\cos\varphi & \sin\theta\sin\varphi & \cos\theta \end{bmatrix} \tag{15}$$

Due to the discretization, some pixels on the boarders of the sensor image cannot be entirely covered by the projected pixels of the spread image. Therefore, this leads to underestimated pixel values. To manage this problem, we eliminate the pixels in the sides of the sensor image that are not entirely filled by the projected pixels of the spread image.

5 Results and validation

5.1 Results and improvements

With the new modelling strategy, conversely to the initial infinite slope mode, scene irradiance is spatially uniform, spread images have the same shape and dimension for any viewing direction, and energy conservation is ensured during the Earth-Atmosphere radiative coupling. These improvements allow DART to simulate accurate RS signals of sloping landscapes. In addition, image accuracy is further improved thanks to the new projection method instead of the previous bi-linear interpolation method. Here, these results are illustrated with DART simulations of the same scenes as in section 3.2 (Figure 7, Figure 8). As expected, the issues previously noted are corrected. For the solo slope scene, the intercepted energy flux is spatially constant (Figure 14.b) and reflectance in the solar plane is constant (Figure 14.c). Also, all sensor images have a correct visual aspect (Figure 15.b-f): no more microgrooves, border effect, and over or underestimated radiance values in parts of the images. Improvements on the intercepted energy flux $\sum_z W(i,j,z)$ (W/µm) per pixel (i,j) and the scene average reflectance $\rho(\theta_v)$ in the solar plane $\varphi_v = 225°$ per zenith angle, with a step $\Delta\theta_v = 1°$, are quantified using two quantities (*i.e.*, absolute relative error $\varepsilon_X(q)$ and mean absolute relative error $\bar{\varepsilon}_X$) defined in equation (16).

$$\varepsilon_X(q) = \frac{|X_{\text{ref}}(q) - X(q)|}{X_{\text{ref}}(q)} \times 100\% \qquad \bar{\varepsilon}_X = \frac{1}{N}\sum_{q=1}^{N} \varepsilon_X(q) \tag{16}$$

where X indicates a type of DART product ($X = \rho$ for reflectance; $X = w$ for intercepted energy flux), $X(q)$ is an element q in X product. Subscript ref is the reference value under the same simulation condition. $\bar{\varepsilon}_\rho$ is the average value of $\varepsilon_\rho(\theta_v)$ for each zenith angle θ_v in the solar plane, and $\bar{\varepsilon}_w$ is the average value of $\varepsilon_w(i,j)$ per pixel (i,j).

The new infinite slope mode is assumed to be the reference. This is fully justified for the solo slope for which results have been computed analytically. For example, the directional reflectance factor of {solo slope with slope normal $\boldsymbol{n}$ and Lambertian reflectance ρ_{ground}} for the sun direction Ω_{sun} (zenith angle θ_{sun}) is $\rho_{\text{ground}} \cdot \frac{|\Omega_{\text{sun}} \cdot \boldsymbol{n}|}{\cos\theta_{\text{sun}}}$ for any viewing direction. Figure 14.c, Figure 16 and Table 3 show the errors in the initial infinite slope mode. For the solo slope scene, $\bar{\varepsilon}_\rho \approx 4.6\%$ and $\bar{\varepsilon}_w \approx 2.8\%$. For the scene of solo slope with a cherry tree, $\bar{\varepsilon}_\rho \approx 4.0\%$ and $\bar{\varepsilon}_w \approx 3.1\%$. Two technical improvements must be noted. (1) The new Lambert azimuthal equal-area projection improves the realism of fisheye image (see Figure 15.d and Figure 8.d). (2) RAM demand and computer time are greatly decreased for oblique slopes. For example, for the "Solo slope + Tree" simulation, RAM demand is reduced by 90% and simulation time is reduced by 10%.

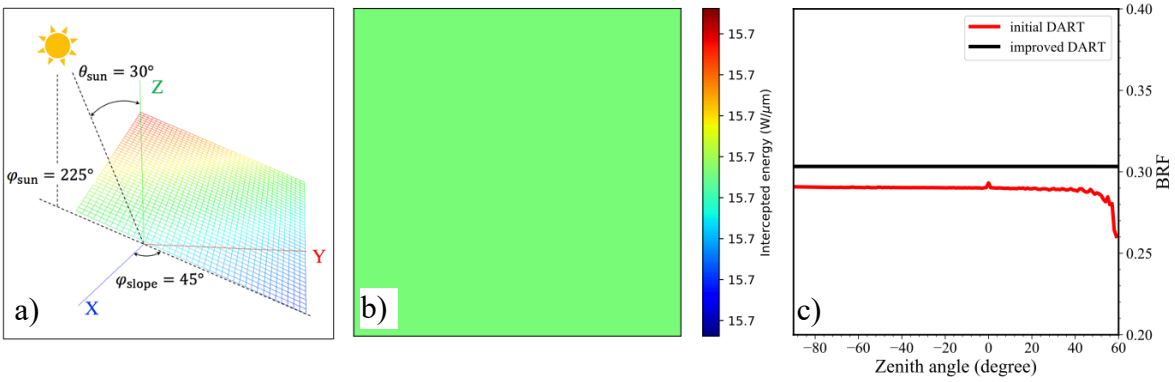

Figure 14. DART simulations with the new infinite slope mode. Solo slope. Same legend as Figure 7.

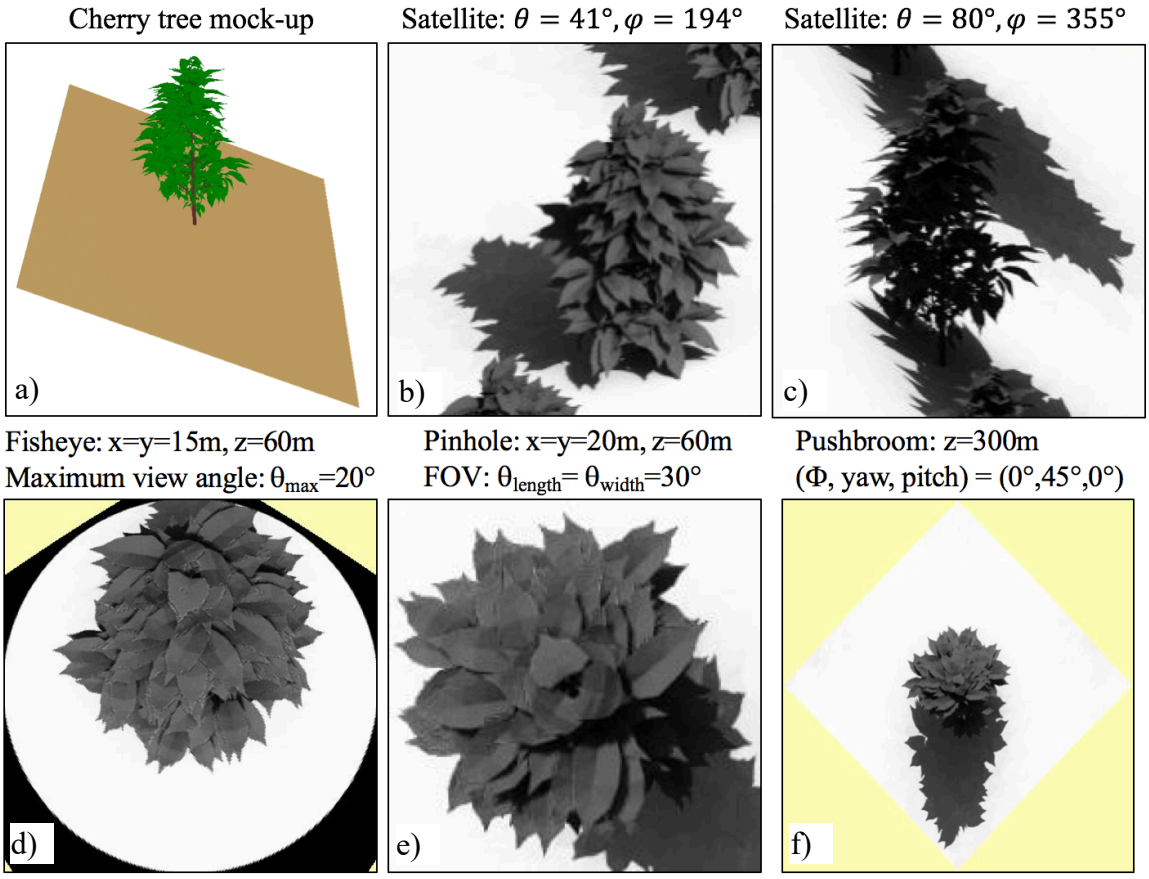

551

552 Figure 15. DART simulations with the new infinite slope mode. Solo slope plus a cherry tree. Same

553 legend as Figure 8.

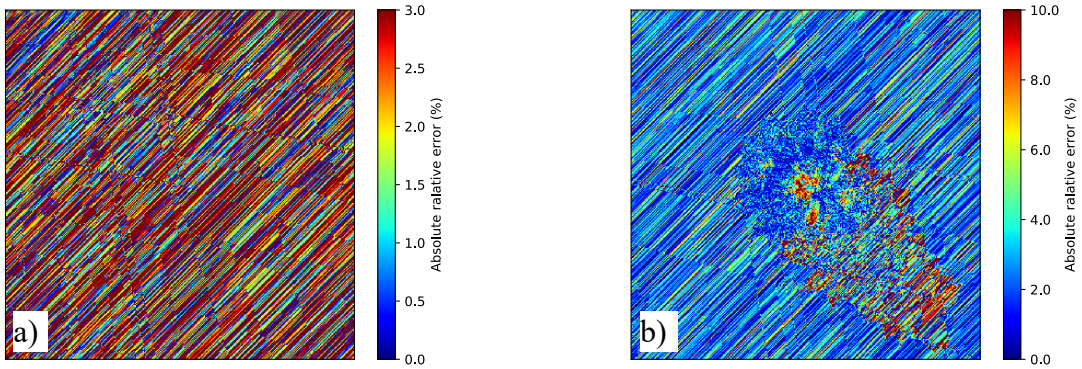

554 Figure 16. Absolute relative error of DART energy flux images (*i.e.*, $\sum_z W(i,j,z)$ (W) per pixel (i,j))

555 simulated with the initial infinite slope mode. a) Solo slope. b) Solo slope with a cherry tree.

Table 3. Summary of the relative error of the initial infinite slope mode for a solo slope and a solo slope with a cherry tree, the results simulated with the new infinite slope are used as reference.

Error	Solo slope	Solo slope + Cherry tree
$\bar{\varepsilon_\rho}$	4.6%	4.0%
$\max(\varepsilon_\rho)$	14.2%	7.0%
$\bar{\varepsilon_w}$	2.8%	3.1%
$\max(\varepsilon_w)$	14.5%	29.9%

5.2 Validation

Ideally, the validation of a modelling approach should be performed with actual measurements. As a first step, here we validate the new modelling strategy of the infinite slope mode using a purely modelling approach. The new DART infinite slope mode is tested with a rugged slope and a rugged slope with realistic forest. For that, two scenes are simulated:

1) Experimental scene: it was simulated with the initial (index init) and new (index new) infinite slope modes.

2) Reference scene: nine duplications of the experimental scene are juxtaposed with respect to the continuity of slopes and altitudes. Its central sub-zone corresponds to the experimental scene, which is called “reference experimental scene” (index ref). Although simulated with the new infinite slope mode, there is no fictive ray tracing (*i.e.*, application of the infinite slope mode) at the borders of the “reference experimental scene”. Therefore, the “reference experimental scene” is used as the reference.

5.2.1 Rugged slope

The rugged slope (Figure 17.a) in the experimental scene (34 m × 34 m) is created by Blender software (www.blender.org). It has relatively large mean altitude shifts: $\Delta Z_X = 15$ m and $\Delta Z_Y = 15$ m along the axes X and Y, respectively. Figure 17.b shows its slope map. The rugged slope has an average slope 38° and a maximum slope 70°. By repeating 9 times the experimental scene with respect to the continuity of slope and altitude, the reference scene (102 m × 102 m) (Figure 17.c) is created, it has mean altitude shifts $\Delta Z_X = 45$ m and $\Delta Z_Y = 45$ m along the axes X and Y, respectively. DART simulations are for a direct sun illumination ($\theta_{\text{sun}} = 40°, \varphi_{\text{sun}} = 300°$), a 0.125 m spatial resolution and a NIR (near infrared: 0.87 µm) spectral band. Ground optical properties are derived from the DART optical properties database. In addition, the roughness of the slope is adjusted by a z-scale factor F_z. For example, $F_z = 2$ means all altitude values in the 3D slope are multiplied by 2. In this study, we investigated 3 rugged slopes with different roughness (F_z = 0.8, 1.0 and 1.2) to assess the robustness of the new method.

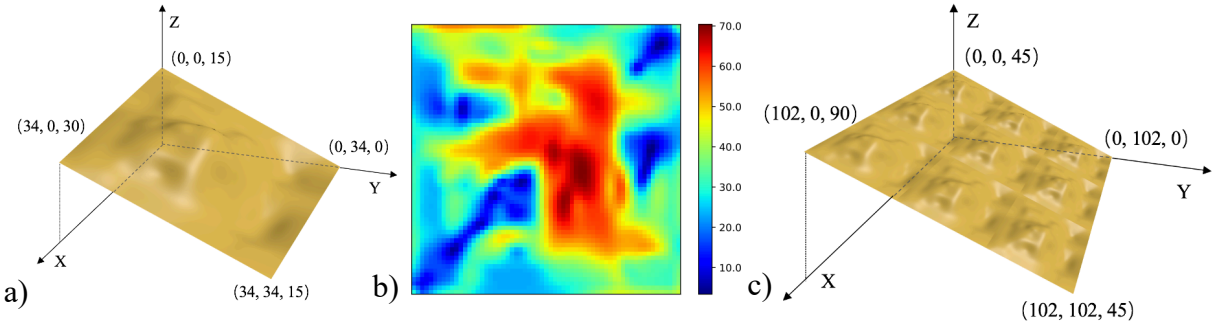

Figure 17. The rugged slope. a) 3D view. b) slope map (unit °). c) 9 duplications of the rugged slope (a) with respect to the continuity of slopes and altitudes.

Figure 18.a, b shows two satellite images simulated with initial infinite slope mode ($F_z = 1.0$), the boarder effect and erroneous areas are obvious. These defects do not appear in the images

simulated by the new infinite slope mode. The microgrooves do not appear in Figure 18.a, b because the variation of pixel reflectance masks the minor reflectance change due to the non-uniform illumination. Figure 18.c, f show the BRFs (*i.e.*, $\rho_{\mathrm{ref}}(\theta_v)$, $\rho_{\mathrm{init}}(\theta_v)$ and $\rho_{\mathrm{new}}(\theta_v)$) in the solar plane (*i.e.* $\varphi_v = 300°$) with zenith angle step $\Delta\theta_v = 2°$ for 3 different z-scale factors (F_z = 0.8, 1.0 and 1.2). They illustrate that the roughness can greatly impact the results of the initial infinite slope mode ($\bar{\varepsilon}_{\rho_{\mathrm{init}}} \approx$ 33.3%, 69.0% and 174.8% for F_z = 0.8, 1.0 and 1.2) whereas it has no impact on the new infinite slope mode ($\bar{\varepsilon}_{\rho_{\mathrm{new}}} < 10^{-4}$ for F_z = 0.8, 1.0 and 1.2). As explained in section 3.1, the BRF in [– 90°, ~ 50°] region is overestimated because the initial method discards total shadow (*i.e.*, apparent reflectance equal to zero) when computing the scene average reflectance (yellow zone in Figure 18.a). For images in the [~ 50°, 90°] region, nearly no shadows are observed. Then, the underestimated BRF is due to the presence of black borders (black lines in Figure 18.b), and mismanagement of image connections (yellow zone in Figure 18.b).

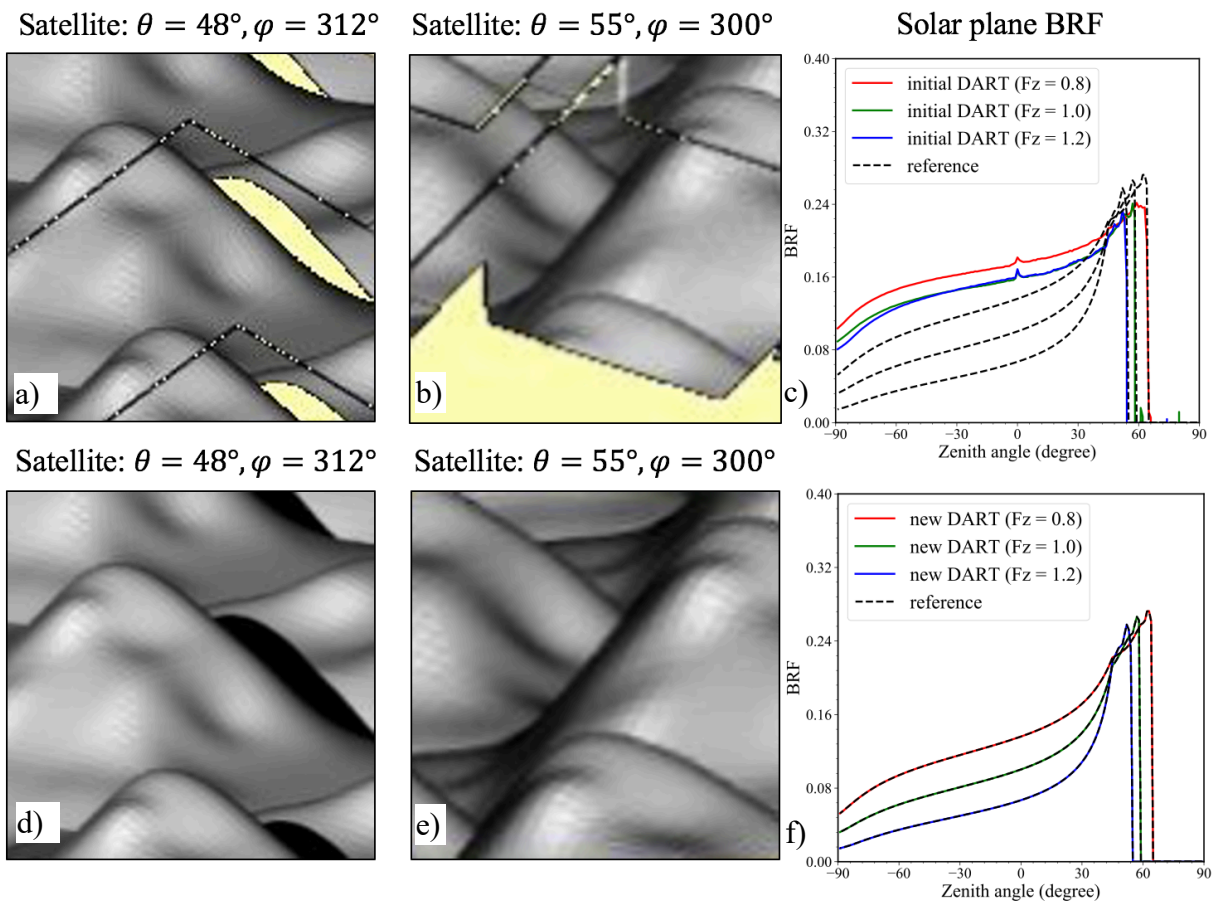

Figure 18. DART simulated satellite images of the rugged slope (experimental scene) with the initial (a, b) and new (d, e) infinite slope modes. The reflectance profile of near infrared band (0.87 µm) in the solar plane are computed for 3 different z-scale factors (F_z = 0.8, 1.0 and 1.2).

5.2.2 Rugged slope with a realistic forest

The scene is a 3D forest over a rugged slope (Figure 17.a). The forest stand is the central part of the Järvselja Birch stand (HET09_JBS_SUM) in RAMI experiment (https://rami-benchmark.jrc.ec.europa.eu). It contains 143 trees with 67 birch trees, 48 linden trees, 13 aspen trees, 5 common alder trees, 5 spruce trees, and 5 ash and maple trees (Figure 19.a). After the duplication of the experimental scene, the reference scene has 1287 trees in total. Figure 19.b

shows the tree spatial distribution in the reference scene. The repetitive pattern of trees can be noted. DEM in the reference scene is the same as Figure 17.c.

DART simulations are conducted with direct sun illumination ($\theta_{\text{sun}} = 40°, \varphi_{\text{sun}} = 300°$), a 0.25 m spatial resolution and 4 spectral bands at NIR (near infrared: 0.87 µm), R (red: 0.66 µm), G (green: 0.57 µm), B (blue: 0.44 µm). Specific optical properties were assigned per tree species. They were simulated by the PROSPECT model using leaf biochemistry parameters obtained by inversion of the optical properties provided by the RAMI experiment (https://rami-benchmark.jrc.ec.europa.eu) (Jacquemoud et al., 1990, Feret et al., 2017). Figure 19.c shows the nadir colour satellite image of the reference scene. A red square outlines the reference experimental scene in the centre.

Figure 19.d shows the BRFs (*i.e.*, $\rho_{\text{ref}}(\theta_v)$, $\rho_{\text{init}}(\theta_v)$ and $\rho_{\text{new}}(\theta_v)$) of the three simulations in the solar plane (*i.e.* $\varphi_v = 300°$) with zenith angle step $\Delta\theta_v = 2°$. Compared to the reference ρ_{ref}, the average absolute relative error of the initial infinite slope mode ρ_{init} is $\bar{\varepsilon}_{\rho_{\text{init}}} \approx 35.4\%$, with maximum absolute relative error $\max(\varepsilon_{\rho_{\text{init}}})$ up to 65.6%. These large error values are mostly due to inaccurate illumination with the strong topography, the mismanagement of image connection and also the fact that pixels in total shadow are discarded when computing the scene average radiance (cf. section 3.1). As expected, the new infinite slope mode greatly improves the situation: $\rho_{\text{new}}(\theta_v) \approx \rho_{\text{ref}}(\theta_v)$ with $\bar{\varepsilon}_{\rho_{\text{new}}} \approx 0.01\%$. Pixel-wise comparison of the nadir radiance images $L(i,j)$ at NIR band between the experimental scene and the reference experimental scene is shown in Figure 19.e and Figure 19.f, respectively for scatter plot "$L_{\text{ref}}(i,j)$, $L_{\text{init}}(i,j)$" and scatter plot "$L_{\text{ref}}(i,j)$, $L_{\text{new}}(i,j)$". Radiance values "$L_{\text{ref}}(i,j)$, $L_{\text{init}}(i,j)$" are very scattered in Figure 19.e. It is consistent with the relatively low coefficient

of determination $R^2 \approx 0.935$. The radiance intercept 0.13 and slope 0.97 indicates the tendency to overestimate radiance in shadow area and to underestimate radiance in brilliant area due to non-uniform scene illumination in presence of strong and asymmetric topography. Figure 19.f shows $R^2 > 0.999$, a slope 1.0001 and an intercept as low as 0.0015. The slim difference between the new infinite slope mode and the reference is probably due to DART discretisation (*i.e.* illumination mesh) combined with the limit of double precision (*i.e.* 16 decimal digits). For example, altitude shift ΔZ of 15 m or 45 m can have a double coding inaccuracy of magnitude 10^{-14} in both the experimental scene and the reference scene, which implies slightly different starting points for the illumination rays. As a result, in the mountain forest scene that is simulated with tens of millions of facets, a ray intercepted by a facet edge in the experimental scene could pass through in the reference scene, which leads to very minor difference between few pixels of the experimental and reference scene.

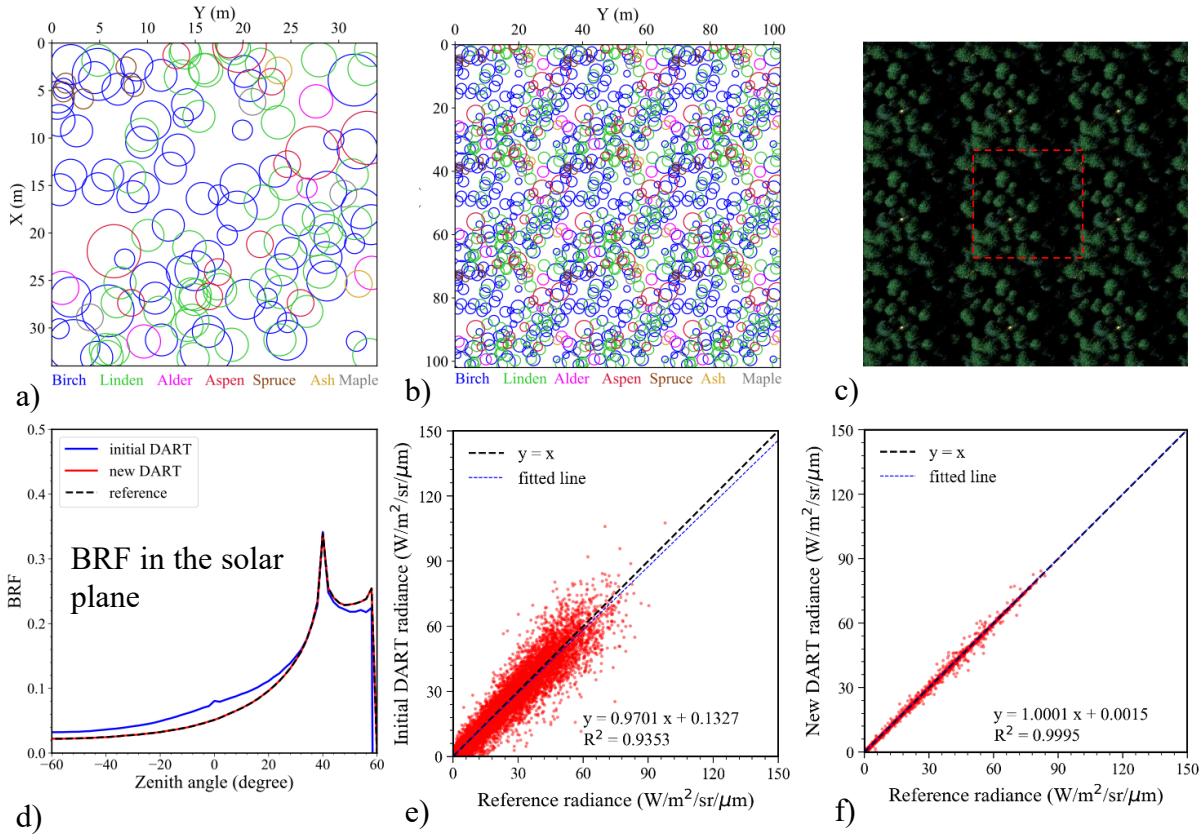

Figure 19. Tree spatial distribution in the experimental (a) and reference (b) scene. c) Nadir colour composite satellite image of the reference scene simulated with the new infinite slope mode. Its central red square outlines the "reference experimental scene". d) NIR BRF in the solar plane for "experimental scene + initial infinite slope mode" (–), "experimental scene + new infinite slope mode" (–) and "reference experimental scene + new infinite slope mode" (- -). Scatter plots of pixel NIR nadir radiance for "Initial - Reference" (e) and "New - Reference" (f).

6 Concluding remarks

This paper presents a new modelling strategy for DART infinite slope mode. This strategy leads to accurate and efficient simulations of RS signals and radiative budget for sloping landscapes. Five key points must be noted: (1) The horizontal atmosphere surface crossed by the upward flux from the landscape or the downward flux from atmosphere is computed per direction in order to ensure energy conservation during the Earth-Atmosphere coupling. (2) The illumination ray-mesh is computed per direction in order to ensure uniform scene illumination for any sloping landscape. (3) The spread images are stored on an oblique plane OP that is topography-adapted instead of the previous horizontal plane HP. It allows DART to generate accurate and high-quality RS images with less RAM demand. (4) Pixels on the spread image are projected on the sensor plane with a precise projection method instead of the bi-linear interpolation method, which further improves the accuracy of the simulated RS image. (5) The Lambert azimuthal equal-area projection is applied to fisheye cameras, which increases the realism of the simulated fisheye images. We simulated four scenarios to assess this improvement:

- Solo slope: the initial infinite slope mode gives the intercepted energy flux map that has a spatial relative variability $(W_{\max}\text{-}W_{\min})/W_{\mathrm{mean}}$ up to 25% and a reflectance relative difference up to 11%. In addition, it underestimates the reflectance in the solar plane by 4.6%. The new infinite slope mode simulates uniform and accurate intercepted energy flux map and BRF.

- Solo slope with a cherry tree: the initial infinite slope mode leads to images with microgrooves, border effects, and erroneous zones. The BRF in the solar plane has an average relative error 4.0% as well. The new infinite slope mode simulates accurate and high-quality RS images without the defects of the initial method.

- Rugged slope: the initial infinite slope mode gives reflectance in the solar plane that has an average relative error up to 69.0%. Indeed, border effects and erroneous zones appear in the simulated images. These errors and defects increase with the slope roughness and obliquity. The new infinite slope improves the accuracy of results with relative error less than 10^{-4} whatever the slope roughness and obliquity. It also simulates accurate and high-quality RS images without defects.

- Rugged slope with a realistic forest: the initial infinite slope mode gives reflectance in the solar plane that has an average relative error up to 35.4%. In addition, the pixel-wise comparison between the reference experimental scene and the experimental scene gives a coefficient of determination R^2 as low as 0.935. Conversely, the new infinite slope mode gives accurate BRF profiles in the solar plane, and a coefficient of determination R^2 larger than 0.999 in the pixel-wise comparison.

In short, these results stress the great improvements of DART infinite slope mode. One should note that the four considered scenarios are a bit extreme because the slopes are relatively large. With less oblique slope, the initial infinite slope mode is less inaccurate.

Current DART infinite slope mode is only available for stratified homogeneous atmosphere. In order to simulate adjacent effect risen by the heterogeneous backscattering, multi-cell in each atmosphere layer should be considered in the future work. Also, the accuracy of this modelling strategy should be assessed through the comparison of DART and satellite images, using field measurements in order to ensure an accurate modelling of the scene.

Acknowledgements

This research is supported by the Occitanie region and by the CNES TOSCA program. We are very thankful to computer scientists Jordan Guilleux and Eric Chavanon in DART team.

Appendix A. Atmosphere backscattering

The backscattered flux is computed by convolving upward radiation from the Earth scene with transfer function $\mathrm{TF}_{\mathrm{BA\text{-}BA}}$, at interface BOA (Grau and Gatellu-Etchegorry, 2013). $\mathrm{TF}_{\mathrm{BA\text{-}BA}}\left(\Delta i, \Delta j, \Omega^{\uparrow}, \Omega'^{\downarrow}\right)$, with $\Delta i = i - i'$ and $\Delta j = j - j'$, gives the flux $W_{\mathrm{BOA}}\left(i', j', \Omega'^{\downarrow}\right)$ that the atmosphere backscatters to pixel (i', j') onto BOA interface for any downward direction $\Omega'^{\downarrow}$, due to unit upward flux $W_{\mathrm{BOA}}\left(i, j, \Omega^{\uparrow}\right)=1$ from pixel (i, j) on BOA interface, along upward

729 direction $\Omega^{\uparrow}$. With an atmosphere spherical albedo $\bar{S}$ and scene albedo ω_{scene}, backscattered
730 energy of infinite coupling order is assumed to be

$$W_{\text{BOA}}^{\text{backscat}}(i', j', \Omega'^{\downarrow}) = \frac{1}{1 - \omega_{\text{scene}} \cdot \bar{S}} \sum_i \sum_j \sum_{\Omega^{\uparrow}} W_{\text{BOA}}^{\text{iter X}}(i, j, \Omega^{\uparrow}) . \text{TF}_{\text{BA-BA}}(\Delta i, \Delta j, \Omega^{\uparrow}, \Omega'^{\downarrow})$$

731 Transfer functions $\text{TF}_{\text{BA-BA}}$, $\text{TF}_{\text{BA}-\text{sensor}}$ and $\text{TF}_{\text{BA-TA}}$ are computed in the atmospheric RT
732 stage. Their use greatly decreases computer time since it avoids repeated RT calculation per
733 pixel. The new infinite slope mode is adapted to the case where each atmosphere MA layer
734 consists of a single cell. Then, pixels (i, j) cannot be distinguished in the backscattering process,
735 and $\text{TF}_{\text{BA}-\text{BA}}(\Delta i, \Delta j, \Omega^{\uparrow}, \Omega'^{\downarrow})$ is simplified as $\text{TF}_{\text{BA}-\text{BA}}(\Omega^{\uparrow}, \Omega'^{\downarrow})$. The flux $W_{\text{BOA}}^{\text{iter X}}(\Omega_n^{\uparrow})$ at BOA
736 level is calculated by subsampling the flux $W_{\text{OP}}^{\text{iter X}}(i, j, \Omega_n^{\uparrow})$ per pixel at OP

$$W_{\text{BOA}}^{\text{iter X}}(\Omega_n^{\uparrow}) = \sum\nolimits_i \sum\nolimits_j W_{\text{OP}}^{\text{iter X}}(i, j, \Omega_n^{\uparrow}) \cdot \frac{S_{\text{scene}}}{S_p(\Omega_n^{\uparrow})}$$

737 with S_{scene} the area of scene horizontal section, $S_p(\Omega_n^{\uparrow})$ the projected surface of OP onto the
738 horizontal atmosphere along direction $\Omega_n^{\uparrow}$.
739
740 It leads to backscattered flux $W_{\text{BOA}}^{\text{backscat}}(\Omega_n^{\downarrow})$ and backscattered flux per pixel ($I_{\text{BOA}} \cdot J_{\text{BOA}}$
741 pixels) at BOA

$$W_{\text{BOA}}^{\text{backscat}}(\Omega_n^{\downarrow}) = \frac{1}{1 - \omega_{\text{scene}} \cdot \bar{S}} \sum\nolimits_{\Omega_n^{\uparrow}} W_{\text{BOA}}^{\text{iter X}}(\Omega_n^{\uparrow}) \cdot \text{TF}_{\text{BA}-\text{BA}}(\Omega_n^{\uparrow}, \Omega_n^{\downarrow})$$

$$W_{\text{BOA}}^{\text{backscat}}(i, j, \Omega_n^{\downarrow}) = \frac{W_{\text{BOA}}^{\text{backscat}}(\Omega_n^{\downarrow})}{I_{\text{BOA}} \cdot J_{\text{BOA}}}$$

742 The atmosphere albedo $\bar{S}$ and backscattered irradiance $E_{\text{BOA}}^{\text{backscat}}$ are calculated as

$$\bar{S} = \frac{\sum_{\Omega_n^{\downarrow}} \sum_{\Omega_n^{\uparrow}} W_{\text{BOA}}^{\text{iter X}}(\Omega_n^{\uparrow}) \cdot \text{TF}_{\text{BA}-\text{BA}}(\Omega_n^{\uparrow}, \Omega_n^{\downarrow})}{\sum_{\Omega_n^{\uparrow}} W_{\text{BOA}}^{\text{iter X}}(\Omega_n^{\uparrow})}, E_{\text{BOA}}^{\text{backscat}} = \frac{\sum_{\Omega_n^{\downarrow}} W_{\text{BOA}}^{\text{backscat}}(\Omega_n^{\downarrow})}{S_{\text{scene}}}$$

743

744 **Appendix B. Simulation of DART products at sensor level and TOA**

745

746 The Earth surface RT of atmosphere backscattered radiance (step 4 in Figure 2) gives
747 $W_{\mathrm{OP}}^{\mathrm{coupl}}\left(i,j,\Omega_n^{\uparrow}\right)$. Then (step 5 in Figure 2), energies at BOA are transferred to TOA and sensor
748 levels. Fluxes at these levels are calculated using $W_{\mathrm{OP}}^{\mathrm{coupl}}\left(i,j,\Omega_n^{\uparrow}\right)$, direct transmittances
749 $\{\mathrm{T_{BA\text{-}TOA}}, \mathrm{T_{BA\text{-}sensor}}\}$ and transfer functions $\{\mathrm{TF_{BA\text{-}TOA}}\left(\Omega_n^{\uparrow},\Omega_{n'}^{\uparrow}\right), \mathrm{TF_{BA\text{-}sensor}}\left(\Omega_n^{\uparrow},\Omega_{n'}^{\uparrow}\right)\}$
750 (Grau and Gatellu-Etchegorry, 2013) (*i.e.*, step 5 in Figure 2). $\mathrm{TF_{BA\text{-}TOA\ (sensor)}}\left(\Omega_n^{\uparrow},\Omega_{n'}^{\uparrow}\right)$ gives
751 the upward flux $W_{\mathrm{TOA(sensor)}}\left(\Omega_{n'}^{\uparrow}\right)$ per upward direction $\Omega_{n'}^{\uparrow}$ at TOA (sensor) level, due to a
752 unit flux $W_{\mathrm{BOA}}\left(\Omega_n^{\uparrow}\right)=1$ from BOA level along the upward direction $\Omega_n^{\uparrow}$. The energy flux
753 $W_{\mathrm{TOA}}\left(i,j,\Omega_n^{\uparrow}\right)$ per pixel (i,j), in the images ($I_{\mathrm{BOA}}\cdot J_{\mathrm{BOA}}$ pixels) per viewing direction $\Omega_n^{\uparrow}$ at
754 TOA and sensor levels is computed as:

755

$$
\begin{aligned}
&W_{\mathrm{TOA}}\left(i,j,\Omega_n^{\uparrow}\right)\\
&=W_{\mathrm{OP}}^{\mathrm{coupl}}\left(i,j,\Omega_n^{\uparrow}\right)\cdot \mathrm{T_{BA-TOA}}\\
&+\frac{W_{\mathrm{TOA}}\left(\Omega_n^{\uparrow}\right)\cdot\frac{S_p\left(\Omega_n^{\uparrow}\right)}{S_{\mathrm{scene}}}+\sum_{\Omega_{n'}^{\uparrow}}\sum_i\sum_j W_{\mathrm{OP}}^{\mathrm{coupl}}\left(i,j,\Omega_n^{\uparrow}\right)\cdot \mathrm{TF_{BA-TOA}}(\Omega_n^{\uparrow},\Omega_{n'}^{\uparrow})}{I_{\mathrm{BOA}}\cdot J_{\mathrm{BOA}}}
\end{aligned}
$$

$$
\begin{aligned}
&W_{\mathrm{sensor}}\left(i,j,\Omega_n^{\uparrow}\right)\\
&=W_{\mathrm{OP}}^{\mathrm{coupl}}\left(i,j,\Omega_n^{\uparrow}\right)\cdot \mathrm{T_{BA-sensor}}\\
&+\frac{W_{\mathrm{sensor}}\left(\Omega_n^{\uparrow}\right)\cdot\frac{S_p\left(\Omega_n^{\uparrow}\right)}{S_{\mathrm{scene}}}+\sum_{\Omega_{n'}^{\uparrow}}\sum_i\sum_j W_{\mathrm{OP}}^{\mathrm{coupl}}\left(i,j,\Omega_n^{\uparrow}\right)\cdot \mathrm{TF_{BA-sensor}}(\Omega_n^{\uparrow},\Omega_{n'}^{\uparrow})}{I_{\mathrm{BOA}}\cdot J_{\mathrm{BOA}}}
\end{aligned}
$$

756 with S_{scene} the area of scene horizontal section, $S_p\left(\Omega_n^{\uparrow}\right)$ the projected surface of OP onto the
757 horizontal atmosphere along direction $\Omega_n^{\uparrow}$.

The backscattered irradiance $E_{\text{sens}}^{\text{backscat}}$ at sensor level is calculated as

$$E_{\text{sensor}}^{\text{backscat}} = \sum_{\Omega_n^{\downarrow}} \sum_{\Omega_n^{\uparrow}} \frac{\sum_i \sum_j W_{\text{OP}}^{\text{coupl}}(i,j,\Omega_n^{\uparrow})}{S_p(\Omega_n^{\uparrow})} \cdot \text{TF}_{\text{BA-sensor}}(\Omega_n^{\uparrow}, \Omega_n^{\downarrow})$$

Associated radiometric products are also computed

$$L_{\text{sensor}}^{\text{coupl}}(i,j,\Omega_n^{\uparrow}) = \frac{W_{\text{sensor}}(i,j,\Omega_n^{\uparrow})}{S_p(i,j,\Omega_n^{\uparrow}) \cdot \cos\theta_n \cdot \Delta\Omega_n^{\uparrow}},\ \rho_{\text{sensor}}^{\text{coupl}}(i,j,\Omega_n^{\uparrow}) = \frac{\pi \cdot L_{\text{sensor}}^{\text{coupl}}(i,j,\Omega_n^{\uparrow})}{E_{\text{sensor}}^{\text{dir}} + E_{\text{sensor}}^{\text{diff}} + E_{\text{sensor}}^{\text{backscat}}}$$

$$L_{\text{TOA}}^{\text{coupl}}(i,j,\Omega_n^{\uparrow}) = \frac{W_{\text{TOA}}(i,j,\Omega_n^{\uparrow})}{S_p(i,j,\Omega_n^{\uparrow}) \cdot \cos\theta_n \cdot \Delta\Omega_n^{\uparrow}},\ \rho_{\text{TOA}}^{\text{coupl}}(i,j,\Omega_n^{\uparrow}) = \frac{\pi \cdot L_{\text{TOA}}^{\text{coupl}}(i,j,\Omega_n^{\uparrow})}{E_{\text{TOA}}^{\text{dir}}}$$

with $L_{\text{sensor}}^{\text{coupl}}$ and $\rho_{\text{sensor}}^{\text{coupl}}$ the radiance and reflectance at sensor level, $L_{\text{TOA}}^{\text{coupl}}$ and $\rho_{\text{TOA}}^{\text{coupl}}$ the radiance and reflectance at TOA. $E_{\text{TOA}}^{\text{dir}}$ is the direct irradiance at TOA. $\Delta\Omega_n^{\uparrow}$ is the solid angle of direction $\Omega_n^{\uparrow}$ and θ_n is the zenith angle of direction $\Omega_n^{\uparrow}$. Superscript "coupl" refers to DART products after the radiative coupling with the atmosphere.

Reference

Anderson, Gail P., et al. *AFGL atmospheric constituent profiles (0.120 km)*. No. AFGL-TR-86-0110. AIR FORCE GEOPHYSICS LAB HANSCOM AFB MA, 1986.

Barrachina, M., Cristóbal, J., & Tulla, A. F. (2015). Estimating above-ground biomass on mountain meadows and pastures through remote sensing. International Journal of Applied Earth Observation and Geoinformation, 38, 184-192.

Berk, A., & Hawes, F. (2017). Validation of MODTRAN® 6 and its line-by-line algorithm. *Journal of Quantitative Spectroscopy and Radiative Transfer*, *203*, 542-556.

Boori, M. S., Voženílek, V., & Choudhary, K. (2015). Land use/cover disturbance due to tourism in Jeseníky Mountain, Czech Republic: A remote sensing and GIS based approach. The Egyptian Journal of Remote Sensing and Space Science, 18(1), 17-26.

Chandrasekhar, Subrahmanyan. *Radiative transfer*. Courier Corporation, 2013.

Chimner, R. A., Bourgeau-Chavez, L., Grelik, S., Hribljan, J. A., Clarke, A. M. P., Polk, M. H., ... & Fuentealba, B. (2019). Mapping Mountain Peatlands and Wet Meadows Using Multi-Date, Multi-Sensor Remote Sensing in the Cordillera Blanca, Peru. *Wetlands*, 1-11.

Denniston, D. (1996). People and mountains. People & the Planet, 5(1).

Fan, W., Chen, J. M., Ju, W., & Zhu, G. (2013). GOST: A geometric-optical model for sloping terrains. *IEEE Transactions on Geoscience and Remote Sensing*, *52*(9), 5469-5482.

Farin, Gerald. Curves and surfaces for computer-aided geometric design: a practical guide. Elsevier, 2014.

Féret, J-B., et al. "PROSPECT-D: towards modeling leaf optical properties through a complete lifecycle." *Remote Sensing of Environment* 193 (2017): 204-215.

Gastellu-Etchegorry, Jean-Philippe, et al. "Modeling radiative transfer in heterogeneous 3-D vegetation canopies." *Remote sensing of environment* 58.2 (1996): 131-156.

802 Gastellu-Etchegorry, Jean-Philippe. "3D modeling of satellite spectral images, radiation budget
803 and energy budget of urban landscapes." *Meteorology and atmospheric physics* 102.3-4 (2008):
804 187.
805
806 Gastellu-Etchegorry, Jean-Philippe, et al. "DART: recent advances in remote sensing data
807 modeling with atmosphere, polarization, and chlorophyll fluorescence." *IEEE Journal of*
808 *Selected Topics in Applied Earth Observations and Remote Sensing* 10.6 (2017): 2640-2649.
809
810 Grau, Eloi, and Jean-Philippe Gastellu-Etchegorry. "Radiative transfer modeling in the Earth–
811 Atmosphere system with DART model." *Remote Sensing of Environment* 139 (2013): 149-170.
812
813 Gu, D., & Gillespie, A. (1998). Topographic normalization of Landsat TM images of forest
814 based on subpixel sun–canopy–sensor geometry. *Remote sensing of Environment*, *64*(2), 166-
815 175.
816
817 Guillevic, P., et al. "Thermal infrared radiative transfer within three-dimensional vegetation
818 covers." *Journal of Geophysical Research: Atmospheres* 108.D8 (2003).
819
820 Guillevic, Pierre C., et al. "Directional viewing effects on satellite land surface temperature
821 products over sparse vegetation canopies—A multisensor analysis." *IEEE Geoscience and*
822 *Remote Sensing Letters* 10.6 (2013): 1464-1468.
823
824 Holben, B. N., & Justice, C. O. (1980). The topographic effect on spectral response from nadir-
825 pointing sensors. *Photogrammetric Engineering and Remote Sensing*, *46*(9), 1191-1200.
826

827 Huang, Huaguo. "Accelerated RAPID Model Using Heterogeneous Porous Objects." *Remote*
828 *Sensing* 10.8 (2018): 1264.
829
830 Jacquemoud, S., and F. Baret. "PROSPECT: A model of leaf optical properties
831 spectra." *Remote sensing of environment*34.2 (1990): 75-91.
832
833 J.-P. Grimaldi and T. Vergauwen, “Luxrender v1.6,” 2008, http://www. luxrender.net/.
834
835 Kallel, Abdelaziz. "Leaf polarized BRDF simulation based on Monte Carlo 3-D vector RT
836 modeling." Journal of Quantitative Spectroscopy and Radiative Transfer 221 (2018): 202-224.
837
838 Liang, S. (2005). Quantitative remote sensing of land surfaces (Vol. 30). John Wiley & Sons.
839
840 Mousivand, A., Verhoef, W., Menenti, M., & Gorte, B. (2015). Modeling top of atmosphere
841 radiance over heterogeneous non-Lambertian rugged terrain. *Remote sensing*, *7*(6), 8019-8044.
842 Price, M. F. (1998). Mountains: globally important ecosystems. UNASYLVA-FAO-, 3-12.
843
844 Pellarin, T., et al. "Three years of L-band brightness temperature measurements in a
845 mountainous area: Topography, vegetation and snowmelt issues." *Remote sensing of*
846 *environment* 180 (2016): 85-98.
847
848 Pharr, M., Jakob, W., & Humphreys, G. (2016). *Physically based rendering: From theory to*
849 *implementation*. Morgan Kaufmann.
850

Proy, C., Tanre, D., & Deschamps, P. Y. (1989). Evaluation of topographic effects in remotely sensed data. *Remote Sensing of Environment*, *30*(1), 21-32.

Qi, J., Xie, D., Guo, D., & Yan, G. (2017). A large-scale emulation system for realistic three-dimensional (3-D) forest simulation. *IEEE Journal of Selected Topics in Applied Earth Observations and Remote Sensing*, *10*(11), 4834-4843.

Qi J., Yin T., Xie D., Gastellu-Etchegorry J.P. 2019. Hybrid Scene Structuring for Accelerating 3D Radiative Transfer. Remote Sensing. Accepted for publication.

Reinhold, S., Belinskiy, A., & Korobov, D. (2016). Caucasia top-down: Remote sensing data for survey in a high altitude mountain landscape. Quaternary International, 402, 46-60.

Richter, R., & Schläpfer, D. (2011). Atmospheric/topographic correction for airborne imagery. *ATCOR-4 user guide*, 565-02.

Sandmeier, S., & Itten, K. I. (1997). A physically-based model to correct atmospheric and illumination effects in optical satellite data of rugged terrain. *IEEE Transactions on Geoscience and Remote Sensing*, *35*(3), 708-717.

Santini, F., & Palombo, A. (2019). Physically Based Approach for Combined Atmospheric and Topographic Corrections. *Remote Sensing*, *11*(10), 1218.

874 Schaaf, C. B., Li, X., & Strahler, A. H. (1994). Topographic effects on bidirectional and
875 hemispherical reflectances calculated with a geometric-optical canopy model. *IEEE*
876 *Transactions on Geoscience and Remote Sensing*, *32*(6), 1186-1193.
877
878 Shettle, Eric P., and Robert W. Fenn. Models for the aerosols of the lower atmosphere and the
879 effects of humidity variations on their optical properties. No. AFGL-TR-79-0214. Air Force
880 Geophysics Lab Hanscom Afb Ma, 1979.
881
882 Teillet, P. M., Guindon, B., & Goodenough, D. G. (1982). On the slope-aspect correction of
883 multispectral scanner data. *Canadian Journal of Remote Sensing*, *8*(2), 84-106.
884
885 Vilfan, Nastassia, et al. "Fluspect-B: A model for leaf fluorescence, reflectance and
886 transmittance spectra." *Remote sensing of environment* 186 (2016): 596-615.
887
888 Wald, I., Woop, S., Benthin, C., Johnson, G. S., & Ernst, M. (2014). Embree: a kernel
889 framework for efficient CPU ray tracing. *ACM Transactions on Graphics (TOG)*, *33*(4), 143.
890
891 Wen, J., Liu, Q., Xiao, Q., Liu, Q., You, D., Hao, D., ... & Lin, X. (2018). Characterizing land
892 surface anisotropic reflectance over rugged terrain: a review of concepts and recent
893 developments. *Remote Sensing*, *10*(3), 370.
894
895 W. Jakob, “Mitsuba: Physically based renderer,” 2014, http://www. mitsuba- renderer.org/.
896

Widlowski, J-L., et al. "Third Radiation Transfer Model Intercomparison (RAMI) exercise: Documenting progress in canopy reflectance models." *Journal of geophysical research: Atmospheres* 112.D9 (2007).

Widlowski, J-L., et al. "The fourth radiation transfer model intercomparison (RAMI-IV): Proficiency testing of canopy reflectance models with ISO-13528." *Journal of Geophysical Research: Atmospheres* 118.13 (2013): 6869-6890.

Widlowski, Jean-Luc, et al. "The fourth phase of the radiative transfer model intercomparison (RAMI) exercise: Actual canopy scenarios and conformity testing." *Remote Sensing of Environment* 169 (2015): 418-437.

Widlowski, Jean-Luc, et al. "Rayspread: A virtual laboratory for rapid BRF simulations over 3-D plant canopies." *Computational methods in transport*. Springer, Berlin, Heidelberg, 2006. 211-231.

List of Figure Captions

Figure 1. DART 3D discrete mock-up. Landscape elements are made of triangles, and/or fluid and turbid vegetation cells. The landscape itself is a cell matrix in order to ease ray tracing. The atmosphere has three levels: upper level made of layers, middle level made of cells of any size, and lower level in the landscape.

Figure 2. Major steps for modelling RT in the Earth-Atmosphere system. Thermal emission in mode (T) is shown by the red symbol (steps 1 and 2). Arrows indicate directly transmitted solar (orange) and thermal (red) radiation, and scattered radiation (yellow), either thermal or solar.

Figure 3. The three DART modes for simulating RT in 3D scenes. a) Isolated scene mode. b) Repetitive scene mode. c) Infinite slope mode. The actually simulated scene is framed by a black box. The dotted box frames one of the fictive neighbourhoods of the actually simulated scene.

Figure 4. DART scene in infinite slope mode with its infinite duplications. Three duplications are shown here. The mean altitude differences between neighbour Earth scenes are indicated (ΔZ_X for axis X and ΔZ_Y for axis Y). DEM Edges are smoothly connected with Bezier triangles.

Figure 5. 2D view of the infinite slope mode RT modelling of initial DART. a) Illumination stage. b) Spread image generation. The scene window for direction Ω_n is the dark blue region at the scene vertical face. Its shape depends on the DEM and the illumination direction. Red arrows are rays in the paper plane. Illumination ray sources start from the scene top and window. Rays that cross scene top / window never re-enter the scene, conversely to rays that cross other parts of the scene vertical face. HP is the horizontal plane that stores the spread images.

Figure 6. Pinhole camera image generation using an interpolation method. a) Projection onto HP of the centre of a pixel in the sensor image. b) Nadir view of the projected point. Δx and Δy are the scale coefficients that vary from 0 to 1.

Figure 7. Simulation of a solo slope, using the initial infinite slope mode. DEM mesh with indication of slope azimuth angle φ_{slope}, and zenith and azimuth angles (θ_{sun}, φ_{sun}) of the direction in which the sun is seen from the Earth surface (a), φ is anticlockwise from South. Solo slope: spectral energy flux map (b) and angular reflectance in the solar plane (c).

Figure 8. Simulation of a cherry tree on a solo slope, using the initial infinite slope mode. Satellite (orthographic) camera images (b, c) with 2 viewing directions, fisheye camera image (d), pinhole camera image (e) and pushbroom image (f).

Figure 9. DART infinite slope mode. a) Earth scene and its fictive oblique plane OP at the scene bottom. b) DEM altitude differences are ΔZ_X along axis X and ΔZ_Y along axis Y axis. c) Projected surface (blue parallelogram) $\Sigma_p(\Omega_n)$ of OP along direction Ω_n onto the horizontal plane that contains the highest point of OP, it has an area equal to $S_p(\Omega_n)$.

Figure 10. 2D (a) and 3D (b) views of the scene illumination stage. $\Sigma_{\text{BOA}}(\Omega_n)$ is the projected surface of OP onto the horizontal BOA plane with backward ray tracing method; its area is $S_p(\Omega_n)$. After atmospheric RT modelling, rays through $\Sigma_{\text{BOA}}(\Omega_n)$ along direction Ω_n illuminates the scene. $P_{\text{ray}}(x, y, z)$ (**x**) is the source point of an incident ray, on the scene top or scene window. $P_{\text{OP}}(x, y, z)$ (x) is the projection on OP of $P_{\text{ray}}(x, y, z)$ along incident direction Ω_n.

Figure 11. Ray projection on OP. a) The red triangle gives rise to a ray along direction $\boldsymbol{r}$ (red arrow) that reaches the scene top. The green triangle is its projection onto OP. P is the projection on OP of a corner l_0 of the red triangle. d is the distance $\|P - l_0\|$. P_0 is the highest

968 point of OP. b) Parallel projection for the orthographic camera and perspective projection for
969 the perspective camera. c) Nadir view of the projected triangle on OP and its break-down into
970 four polygons.
971
972 Figure 12. Projection processes for simulating images. Parallel projection along direction Ω_n
973 for satellite (orthographic) camera (a), and perspective projection along local viewing direction
974 for pinhole camera (b) and pushbroom camera (c).
975
976 Figure 13. Projection processes for simulating fisheye images. First, pixel on OP is projected
977 onto a unit sphere. Then, it is spread on the sensor plane with Lambert azimuthal equal-area
978 projection method that projects a point (x, y, z) of the unit sphere onto the sensor plane at point
979 (X, Y, Z). $\theta_{\max}$ is the maximum viewing zenith angle.
980
981 Figure 14. DART simulations with the new infinite slope mode. Solo slope. Same legend as
982 Figure 7.
983
984 Figure 15. DART simulations with the new infinite slope mode. Solo slope plus a cherry tree.
985 Same legend as Figure 8.
986
987 Figure 16. Absolute relative error of DART energy flux images (*i.e.*, $\sum_z W(i, j, z)$ (W) per pixel
988 (i, j)) simulated with the initial infinite slope mode. a) Solo slope. b) Solo slope with a cherry
989 tree.
990
991 Figure 17. The rugged slope. a) 3D view. b) slope map (unit °). c) 9 duplications of the rugged
992 slope (a) with respect to the continuity of slopes and altitudes.

Figure 18. DART simulated satellite images of the rugged slope (experimental scene) with the initial (a, b) and new (d, e) infinite slope modes. The reflectance profile of near infrared band (0.87 µm) in the solar plane are computed for 3 different z-scale factors (F_z = 0.8, 1.0 and 1.2).

Figure 19. Tree spatial distribution in the experimental (a) and reference (b) scene. c) Nadir colour composite satellite image of the reference scene simulated with the new infinite slope mode. Its central red square outlines the "reference experimental scene". d) NIR BRF in the solar plane for "experimental scene + initial infinite slope mode" (–), "experimental scene + new infinite slope mode" (–) and "reference experimental scene + new infinite slope mode" (- -). Scatter plots of pixel NIR nadir radiance for "Initial - Reference" (e) and "New - Reference" (f).